Stability Enhancement of Atomic Timekeeping
Using Raman Adiabatic Rapid Passage

by

Nancy Y. Wu

B.S., Applied Physics

California Institute of Technology (2014)

Submitted to the Department of Aeronautics and Astronautics
in partial fulfillment of the requirements for the degree of

Master of Science in Aeronautics and Astronautics

at the

MASSACHUSETTS INSTITUTE OF TECHNOLOGY

June 2017

Signature redacted

Author . . . . , ...
Department of Aeronautics and Astronautics
May 25, 2017

Signature redacted

Certified by . . . .
/
Richard E. Stoner
Laboratory Technical Staff, C.S. Draper Laboratory

Signature redacted   Thesis Supervisor

Certified by . . . .
Paulo C. Lozano
R.L. Bisplinghoff Professor of Aeronautics and Astronautics
Thesis Supervisor

Signature redacted

Accepted by . . . .
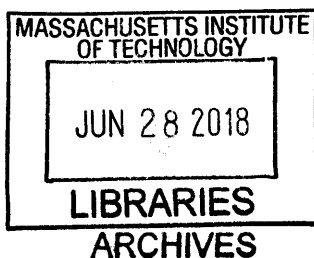(
Youssef M. Marzouk
Associate Professor of Aeronautics and Astronautics
Chair, Graduate Program Committee

Stability Enhancement of Atomic Timekeeping Using Raman Adiabatic Rapid Passage

by

Nancy Y. Wu

Abstract

Current state-of-the-art atomic clocks span the range from large accurate fountain clocks such as the NIST-F2 to relatively small inaccurate chip scale clocks. Small clocks with higher accuracy could greatly expand the range of applications for precision timekeeping, and enable cheaper implementation of existing applications. This type of clock may be realized by use of optical Raman interferometry based on pulsed interrogation of cold atoms. However, this method suffers from serious systematic error sources, e.g., AC Stark shift and Zeeman shift, which alter the atomic resonance frequency. A new method based on adiabatic rapid passage (ARP) has been recently demonstrated at Draper which has significantly reduced phase sensitivity to differential AC Stark shift. It is found that compared to standard Raman, use of ARP enhances timekeeping stability by a factor of three with stability of 2×10^{-12} at 100 seconds. Increasing data rate may also improve short term stability. With all of the above improvements, ARP enhances short term fractional stability to 7×10^{-12} at one second.

Thesis Supervisor: Richard E. Stoner
Title: Laboratory Technical Staff, C.S. Draper Laboratory

Thesis Supervisor: Paulo C. Lozano
Title: R.L. Bisplinghoff Professor of Aeronautics and Astronautics

Acknowledgments

Coming into grad school, I was excited and a bit nervous to work with two advisors, Dr. Rick Stoner and Professor Paulo Lozano. However, I slowly found my nervousness to be entirely misplaced.

I'd hoped for once a month meetings, at least–Rick met with me every *day*. He gave me detailed explanations in response to my questions, performed light speed mental math acrobatics, and provided insightful analyses of my data. At the end of our daily meeting, he spent time getting his hands dirty in the lab, regaling me with cautionary tales from his grad school days on the strength of BNC cables and the deformability of magnetic shields. He gave me highly effective pep talks when things weren't going smoothly, and taught me to be "satisfied with my progress." And just as importantly, he listened to not only my lab concerns, but also those related to my coursework, housing and other stressful situations that the storm of grad school threw at me. Away from my closest friends and family, Rick was my academic father and buoyed me up at the most difficult time in my life.

I got to know Paulo more through the classes I took from him each semester. His excitement for his subject was infectious, and he personally held office hours for his classes, during which none of my stupid questions were unanswered. Paulo's door was always open, and he always greeted me with a smile and asked how I was with genuine interest in my answer. He and Rick were the most supportive and kind advisors I could have hoped for.

My coworkers at Draper were like my family away from home. Nicole Pomeroy held my hand for the first month, showing me the ropes and teaching me how to take data with the sprawling LabVIEW interface. As the previous owner of the cold atom test bed in 1314N, she swiftly diagnosed my newbie user errors and offered quick fixes. I could always count on her for thorough and sincere explanations to my questions. Krish Kotru, in whose footsteps my research follows, was patient in sharing his knowledge and providing expert insight into the more physical aspects of cold atom interferometry. As we were once the two students in the group, I felt a

certain kinship with him which manifested in late night stays and weekend work. I would like to thank him especially for the very thorough reading and copious feedback on this thesis as well. Justin Brown could provide the answer to my every question and its follow-up, and was an invaluable source of knowledge, energy, and wit. Brian Timmons, cold atom guru and architect of the LabVIEW software, got me to delve into the guts of the code and was an enormous help in overhauling the experiment sequence to run more accurately. Jen Choy, despite working on an entirely different project, was extremely kind and always willing to help. In the course of my work, she allowed me to borrow many tools and equipment from her. I must thank all of these wonderful people, in addition to Dave Butts (who has gone to the dark side), Dave Johnson, and Sungyung Lim for their invaluable guidance and camaraderie.

I would also like to thank the Draper Education Department, and MIT AeroAstro for funding my research.

This thesis would not have been possible without the additional support of my "supervisor" Hairy. His green furry face and determined stare were enough to spur me on in difficult times.

Lastly, I would like to thank my parents for their loving, steadfast support. I could not have finished this without them.

. . . .

Nancy Wu

Contents

List of Figures

Chapter 1

Introduction

A clock is composed of an oscillator and a counter, telling time by counting the cycles of an oscillator such as a swinging pendulum. Over the past centuries, the search for stable and precise oscillators has advanced from pendulums to quartz crystals to atoms. No two pendulums or quartz crystals are exactly identical due to their inherent material differences, which translates to timekeeping differences. In contrast, all the atoms of a specific element and isotope are the same, which translates to more accurate, reproducible timing. For reference, the timekeeping uncertainty in an interval of 24 hours is about 10 seconds for a pendulum, 10 microseconds for a quartz crystal, and 1 nanosecond for a atomic cesium beam clock [2]. Thus, atomic clocks are the main focus of this thesis.

Quartz crystal clocks are sufficient for daily life and many laboratory instruments. However, several applications require the precision and stability of atomic clocks. These include navigation, the global positioning system, distributed networks, communication systems, and laboratory instruments.

1.1   Atomic Clocks and Motivation

A typical atomic clock consists of an atomic oscillator, a local oscillator, and a control loop (Figure 1-1). The principle underlying the atomic oscillator is that all the atoms of a specific element and isotope are identical; these atoms emit or absorb electro-

magnetic waves of the same frequency when they shift between two energy levels. This frequency is called the resonance frequency, which is intrinsic to the atoms and independent of space or time. The relationship between the resonance frequency v_0 and atomic energy levels is expressed as

$$v_0 = \frac{E_2 - E_1}{h} \tag{1.1}$$

Where E_1 and E_2 represent two energy levels of the atom, and h is Planck's constant.

Traditionally, alkali metals such as rubidium and cesium are chosen for atomic timekeeping, since they have a relatively simple atomic energy level structure, with only one valence electron. Their ground state is split into two hyperfine levels which are separated by a microwave frequency. This frequency is used as the oscillator frequency in atomic clocks.
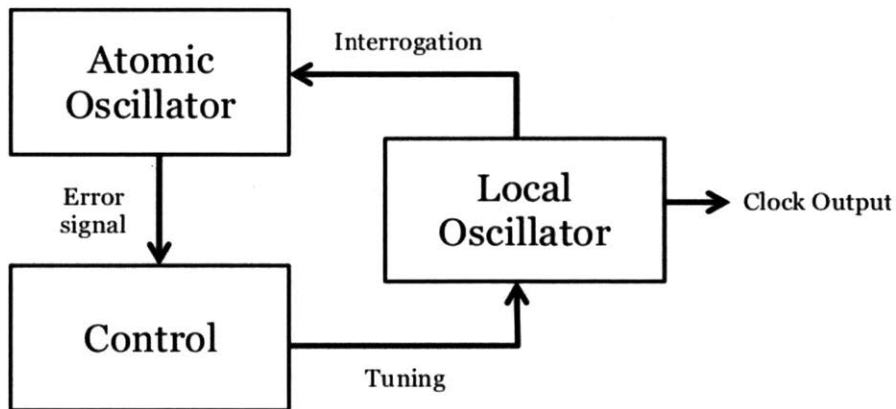
Figure 1-1: Block diagram showing the principal components of an atomic clock: local oscillator, atomic oscillator and control loop. The local oscillator is periodically calibrated by atomic oscillator through control loop. The time output reflects the accuracy and stability of atomic oscillator instead of local oscillator.

For clocks based on alkali ground state transitions, the local oscillator is generally a quartz crystal, and a microwave frequency is synthesized from it to interrogate the atoms. If the synthesized microwave frequency is not the same as the atomic resonance frequency, an error signal is generated, and the controller will correct the local oscillator to match the resonance frequency of the atoms. Thus, the timekeeping

output from the local oscillator is determined by the atoms, not by the quartz crystal local oscillator. There is another class of clocks in which the hyperfine states of the atoms are interrogated with optical rather than microwave frequencies, which will be discussed in chapter 2.

There are several varieties of atomic clocks with different stability characteristics and size, weight, and power (SWaP). The international time standard is realized by cold atom fountain clocks such as NIST-F2. These atomic clocks are room-sized devices in environmentally controlled laboratories. They are highly accurate and stable, and the NIST-F2 only drifts by one second in 0.44×10^{15} seconds[1] [3]. Fountain clocks achieve their high timing accuracy by launching a large number of cold atoms upwards in a cavity (1.5 m high in the NIST-F2). This increases the amount of time that may be used to interrogate the atoms, which in turn improves the precision with which the resonance frequency can be measured. In NIST-F2, the resonance frequency is probed with microwaves.

Chip-scale atomic clocks (CSACs) are the most compact atomic clocks. The commercially available CSAC, the Microsemi Quantum^{TM} SA.45s, has a volume of 17 cm^3. Alkali metal vapor is placed in a high-pressure nitrogen buffer gas and probed with laser pulses. The high pressure gas immobilizes the atoms to realize the relatively long time of interrogation, but the pressure (and thus the measured atomic resonance) is highly dependent on ambient temperature variations. These atomic clocks have a fractional frequency stability of 3×10^{-10} at 1 second, [4], which is insufficient for primary references. As a result, CSAC clocks serve as secondary references.

There is a vast application space for atomic clocks that are relatively small in size, with better stability than the CSAC, able to operate in dynamic environments beyond the laboratory. Probing atoms with microwaves requires a bulky microwave cavity, which constrains the size reduction of clocks. A promising solution is to probe the atoms using optical rather than microwave frequencies. However, the large frequency shift due to the collision of alkali atoms with high-pressure buffer gases means

---

[1]About 14 million years. For reference, the age of the universe is 4.25×10^{17} seconds or 14 billion years.

the CSAC is fundamentally too inaccurate for use as a primary reference. Instead of a buffer gas, laser cooling under ultra high vacuum can be used. The resulting cold atoms facilitate longer atomic coherence times, which is ideal for accurate timekeeping (coherence time is the duration over which an ensemble of atoms synchronously oscillate). In addition, the isolation of atoms from the environment and buffer collisions reduces temperature sensitivity. This is the approach taken in this thesis for a compact atomic clock that may be used as a primary reference.

In the apparatus, ultra high vacuum ($\sim 10^{-9}$ Torr) was achieved in a miniature vacuum cell of 80 cm^3. Cesium atoms were vaporized into the vacuum cell and cooled down to microkelvin temperatures in a 3D magneto-optical trap (details in Chapter 3). The cesium atoms were prepared into the requisite ground state and then interrogated with a sequence of laser pulses.

1.2   Atomic Accelerometer

The atomic timekeeping system in this thesis can also be used as a high-precision atomic accelerometer. The principle of an atomic accelerometer can be understood through the kinematic equation of acceleration. The kinematic measurement of acceleration is performed by tracking the position of a moving object at fixed time intervals. For instance, if three positions of the object (z_1, z_2, z_3) are measured with time T between them, then the finite difference estimate of acceleration is expressed as

$$a = \frac{(z_3 - z_2) - (z_2 - z_1)}{T^2} \tag{1.2}$$

Similarly, if an atom undergoes acceleration due to gravity or other inertial input, the atom's displacement can be recorded in terms of phase by atomic interferometry. The phase $\tilde{\phi}_1$, $\tilde{\phi}_2$, and $\tilde{\phi}_3$ may be used to find the three positions (z_1, z_2, z_3; Figure 1-2), and the equation of acceleration is as follows (see Chapter 2 for details):
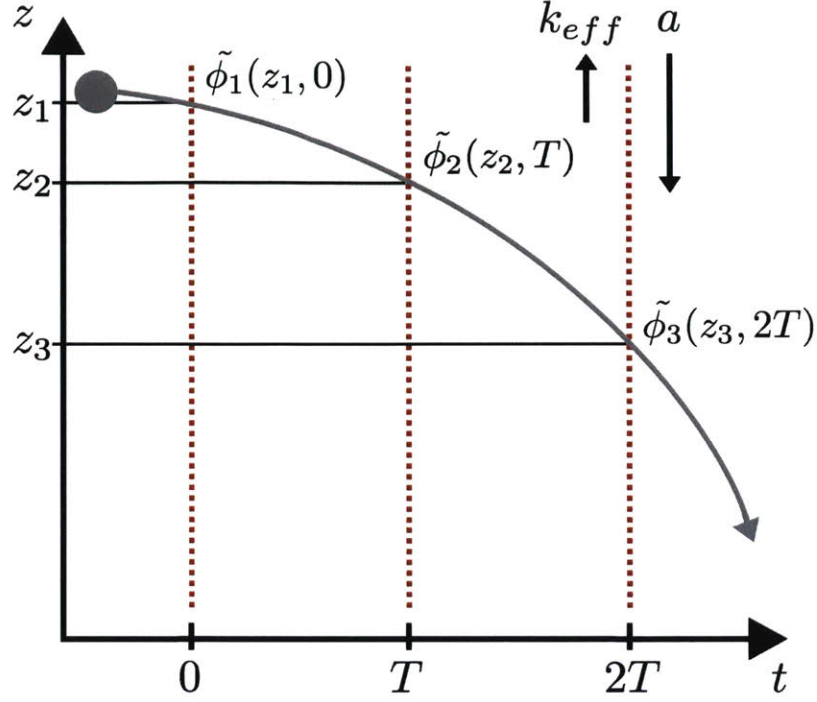
Figure 1-2: An atom with a downward acceleration. Its three positions (z_1, z_2, z_3) are tracked with laser pulses and recorded as three phases ($\tilde{\phi}_1$, $\tilde{\phi}_2$, and $\tilde{\phi}_3$).

$$a = \frac{(\tilde{\phi}_3 - \tilde{\phi}_2) - (\tilde{\phi}_2 - \tilde{\phi}_1)}{k_{eff} T^2} \tag{1.3}$$

Where k_{eff} is the effective wavevector of the interferometer laser beams and T is the time interval between the measurements.

1.3   Interrogation of Atoms with Laser Pulses

Two approaches to interrogating atoms with lasers for atomic timekeeping are coherent population trapping [5] and stimulated Raman transitions [6]. For coherent population trapping, two lasers are coupled to a three-level quantum system with ground states $|g\rangle$ and $|e\rangle$ and excited state $|i\rangle$ (Figure 1-3). When the frequency difference between the two lasers exactly matches the resonance frequency between

two hyperfine levels, a population of atoms in a coherent superposition principally comprising two lower states $|e\rangle$ and $|g\rangle$ is obtained; this is known as the two-photon resonance. This resonance is manifested by a narrow peak in the optical transparency of the atomic sample. We call this the coherent superposition of ground states the "dark state" because its interaction with the laser is suppressed. The dark state only occurs at a very narrow range of differential resonance frequencies, which enables high precision measurements; the CSAC exploits a dark state resonance as its atomic reference.
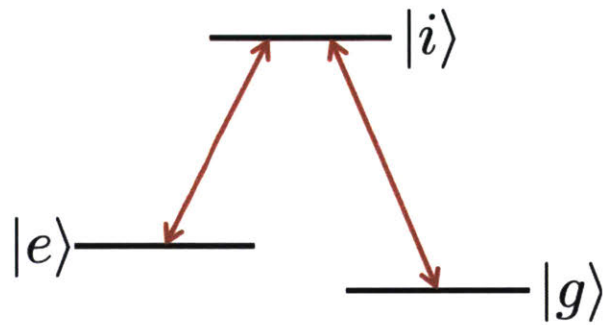
Figure 1-3: Schematic diagram showing the coupling of lasers and atomic states for coherent population trapping scheme. The $|g\rangle$ and $|e\rangle$ represent two hyperfine ground states, and $|i\rangle$ is the excited state. Double red arrows are two laser beams.

The stimulated Raman scheme differs from coherent population trapping by a large detuning of both lasers from the excited state (Figure 1-4). This detuning is between 2 to 4 GHz, and suppresses spontaneous emission as well as coherent population trapping. Stimulated Raman transitions also require that the frequency difference between the two lasers matches the atomic resonance frequency between two hyperfine ground states. Raman transitions shift an atom in ground state $|g\rangle$ to $|e\rangle$ by having the atom simultaneously absorb a photon of momentum $\hbar k_1$ and emit a photon of momentum $\hbar k_2$. The emitted photon has the same phase, frequency, polarization and travel direction as the incident k_2 photon. In contrast, photons from spontaneous emission travel in random directions and may have a different frequency.

However, complications may arise from the use of stimulated Raman transitions. The interaction between laser pulses and cesium atoms may change the atomic resonance frequency through the AC Stark effect. The presence of magnetic fields splits
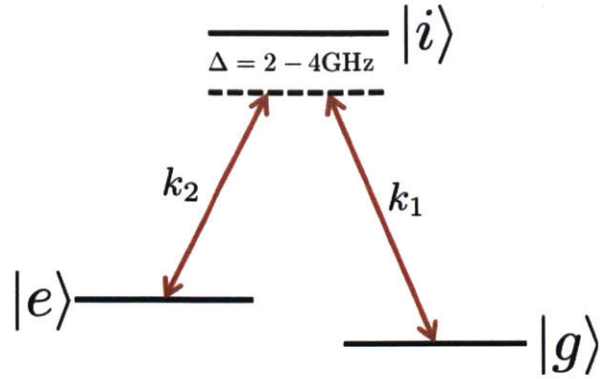
Figure 1-4: Schematic diagram showing the configuration of two lasers and atomic states for stimulated Raman transition. The $|g\rangle$ and $|e\rangle$ represent two hyperfine ground states, and $|i\rangle$ is the excited state. The two laser beams are indicated by k_1 and k_2.

the hyperfine levels further into several magnetically sensitive sublevels due to the Zeeman effect. In addition to field effects, fast-moving atoms are also subject to the Doppler effect, which causes the atoms to see a higher or lower laser frequency depending on their travel direction.

In order to suppress the above effects and other undesirable factors, various optimized schemes have been proposed to interrogate the atoms. Raman adiabatic rapid passage (ARP) for the purpose of timekeeping was recently developed at Draper Laboratory [7]. It has been shown that Raman ARP can significantly suppress the Ramsey phase sensitivity to the AC Stark shift in comparison with the standard Raman transition.

The first aim of this thesis is to further investigate the stability of atomic timekeeping using Raman ARP in comparison with the standard Raman transition. The second objective is to explore the ARP stability improvement with magnetic shielding because the original study of Raman ARP was not magnetically shielded [8]. The third goal is to enhance the stability through other approaches such as increasing the data-rate.

1.4   Thesis Contribution

Significant amount of time was spent on design, construction, characterization, optimization, and trouble-shooting of the apparatus. Several contributions are summarized as follows:

1. The stability of Raman pulse-based atomic timekeeping was enhanced by a factor of ~ 3 by using ARP instead of the standard Raman transitions.

2. Magnetic shielding improved the ARP stability by a factor of 2 to 3.

3. Increasing the data rate also enhances stability. The experimental results show that adopting a high data rate of 6.25 Hz enhanced stability by a factor of about 1.5 in comparison with a data rate of 3.2 Hz.

4. The Allan deviation (see section 4.1.3) of our timing apparatus is about 7×10^{-12} at 1 second and 2×10^{-12} at 100 seconds, which are more than one order of magnitude better than the stability (about 3×10^{-10} at 1 second and 3×10^{-11} at 100 seconds) of CSAC clocks [4]. Our result is five times better than that of a cold atom double-Λ coherent population trapping clock, which has Allan deviation of 4×10^{-11} at 1 second and 4×10^{-12} at 100 seconds [9].

1.5   Thesis Outline

This thesis is mainly focused on the stability enhancement of compact atomic timekeeping for a primary reference. Chapter 2 reviews the theory and principles, which include cesium energy levels, standard and ARP Raman transitions, and Ramsey interferometry. Chapter 3 describes the major components of the apparatus and their functions, especially the magneto-optical trap system, optical system, and magnetic shielding. Chapter 4 presents experimental stability results when using ARP, standard Raman, magnetic shielding, and high data rates. Chapter 5 summarizes the results and suggests future work.

Chapter 2

Principles and Theory

Cesium has well-defined hyperfine structure, which makes it popular for atomic time-keeping and other atomic optics. First, the fine and hyperfine structures of cesium are outlined briefly. Then, Raman transitions are discussed, as well as Raman Adiabatic Rapid Passage. Finally, these are placed in the context of atom interferometry for the purpose of atomic timekeeping and accelerometry.

2.1   Cesium Fine and Hyperfine Structure

Cesium has only one electron in the outermost $6S$ shell; its other shells are full up to $5P$ ([Xe] $6s^1$). The energy level structure of cesium is shown in figure 2-1. Energy levels $6^2S_{1/2}$, $6^2P_{1/2}$, and $6^2P_{3/2}$ are further split by hyperfine structure and magnetic sublevels. [10]. The transition $6^2S_{1/2} \rightarrow 6^2P_{1/2}$ is the so-called D_1 line transition, and $6^2S_{1/2} \rightarrow 6^2P_{3/2}$ is the D_2 line transition. The frequencies corresponding to the D_1 and D_2 line transitions are 335 THz and 352 THz, respectively.

The fine structure energy is specified by the total electron angular momentum $\vec{J}$.

$$\vec{J} = \vec{L} + \vec{S} \qquad (2.1)$$

where $\vec{L}$ is its orbital angular momentum and $\vec{S}$ is its spin angular momentum. Usage of $\vec{J}$ is preferred due to spin-orbit ($\vec{L}$ and $\vec{S}$)coupling. The values of $\vec{J}$ are
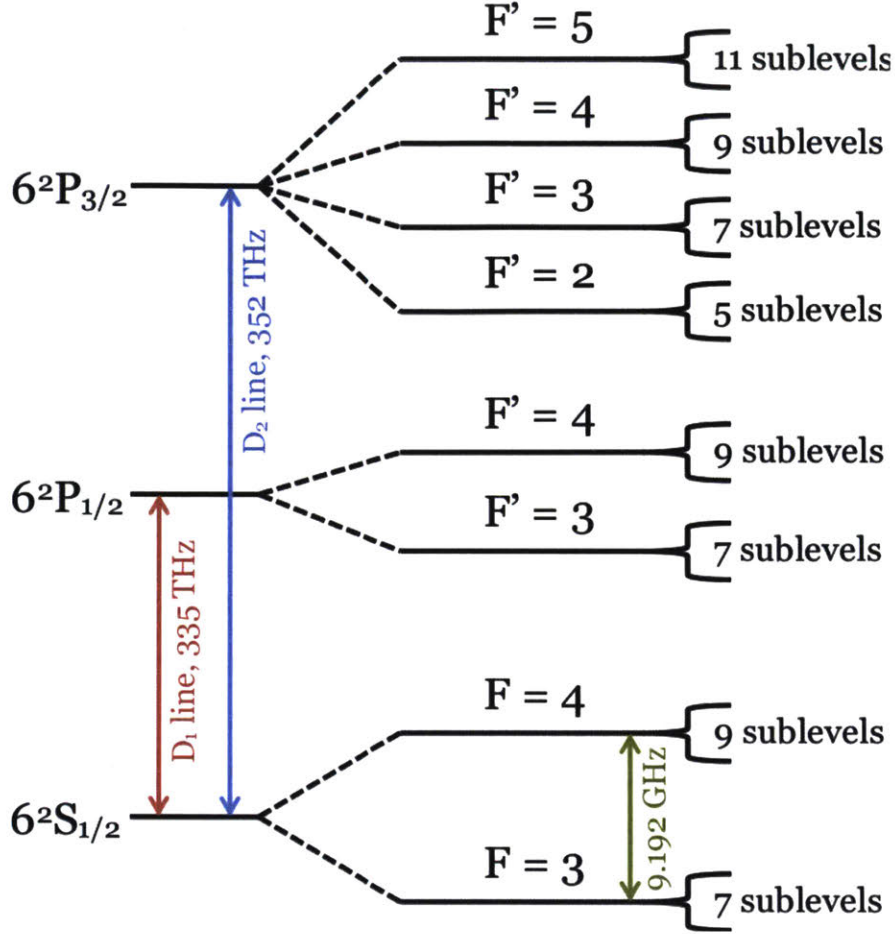
Figure 2-1: Energy level structure of cesium, fine and hyperfine structure and Zeeman splitting. The energy level splittings are not drawn to scale.

defined as follows

$$|L - S| \leq J \leq L + S \tag{2.2}$$

Standard notation denotes the quantum numbers for a state as $N^{2S+1}L_J$. For the cesium ground state ($6^2S_{1/2}$), L = 0, S = 1/2, J = 1/2. For the excited states ($6^2P_{1/2}, 6^2P_{3/2}$), L = 1, S = 1/2, J = 1/2 or 3/2.

Based on the total atomic angular momentum $\vec{F}$, the cesium fine structure levels are split into multiple hyperfine structure levels of ground states F and excited states F'

$$\vec{F} = \vec{I} + \vec{J} \tag{2.3}$$

24

Where $\vec{I}$ is the total nuclear angular momentum, and $\vec{J}$ is the total electron angular momentum. The values of F are as follows

$$|I - J| \leq F \leq I + J \qquad (2.4)$$

Cesium has a nuclear angular momentum of 7/2. For the ground state $6^2S_{1/2}$, F = 3 or 4. For the excited state $6^2P_{1/2}$, F' = 3 or 4, and for the excited state $6^2P_{3/2}$, F' = 2, 3, 4, or 5 (Figure 2-1).

In the presence of magnetic fields, each hyperfine level splits into several magnetic sublevels due to the Zeeman Effect. In the limit of low magnetic field, the number of magnetic sublevels is equal to 2F + 1, e.g., for the F = 4 ground state, there are 9 sublevels ($m_F = \pm 4, \pm 3, \pm 2, \pm 1$ and 0). These sublevels are degenerate if external magnetic fields are absent. However, the degeneracy is lifted if a magnetic field is applied. Experiments in this thesis were conducted in the low field limit.

The hyperfine ground states of cesium are of central importance for atomic time-keeping. The current definition of the SI second is "the duration of 9 192 631 770 periods of the radiation corresponding to the transition between the two hyperfine levels of the ground state of the cesium 133 atom" [2].

Although all alkali metals have a fairly simple electronic structure with only one electron in the outer shell, the cesium ground states (F = 3 and F = 4) have the largest separation, which tends to yield better stability. The performance figure of merit for timekeeping is fractional frequency stability $\Delta\nu/\nu$: for a given timekeeping modality, systematic errors and noise processes tend to be comparable in magnitude for different alkali species, so a larger transition frequency tends to improve factional stability. Cesium has an additional advantage as a heavier alkali metal. In systems using cold atoms, heavier atoms have lower thermal velocities at a given temperature, which allows for longer coherence times.

2.2 Stimulated Raman Transition

In order to drive transitions between the two hyperfine ground states (F = 3 or $|g\rangle$, and F = 4 or $|e\rangle$) spaced by microwave frequency ω_{HFS}, one approach is to directly apply microwaves to the atoms; however, microwave interrogation requires relatively large cavities that can significantly increase the apparatus size. An alternative method is to use laser pulses to realize the above transition; stimulated Raman pulses and Raman adiabatic rapid passage pulses were explored in this thesis.

Stimulated Raman transitions use two lasers to irradiate a three-level quantum system. In the case of cesium, the three-level system consists of two ground states ($|g\rangle$ and $|e\rangle$) and excited state $|i\rangle$ (Figure 2-2).
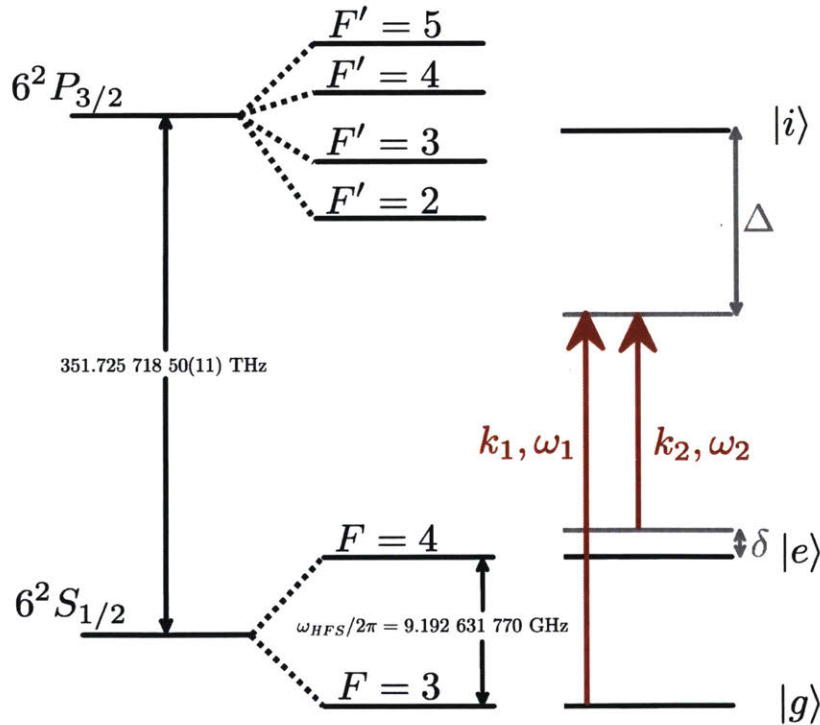
Figure 2-2: Stimulated Raman transition of cesium atoms on the D_2 line. Two Raman lasers with frequencies ω_1 and ω_2 are detuned from the intermediate excited state $|i\rangle$ by -2 to -4 GHz. The difference between the hyperfine frequency ω_{HFS} and the Raman laser frequency offset ($\omega_1 - \omega_2$) is called the Raman detuning δ.

To suppress spontaneous emission, both Raman laser frequencies are detuned from the intermediate state $|i\rangle$ by a frequency $\Delta = -2$ to -4 GHz. The Δ values should be much larger than the $6^2S_{1/2}$ to $6^2P_{3/2}$ transition linewidth of 5.2 MHz in cesium [10]. However, it must also avoid the hyperfine splitting frequency of 9.2 GHz, otherwise single-photon processes may occur. For example, if the Raman laser with frequency ω_1 is detuned from $|i\rangle$ by 9.2 GHz, then it would excite the $|e\rangle$ atoms into state $|i\rangle$ and trigger spontaneous emission (Figure 2-2).

When the frequency difference between the two lasers matches or is very close to the atomic resonance frequency between two hyperfine ground states, the cesium atom in ground state $|g\rangle$ transits into ground state $|e\rangle$ after absorbing a k_1 photon and emitting a k_2 photon identical to the incident k_2 photon.

Stimulated Raman transitions are cyclic (i.e, Rabi cycling); the probability of an atomic transition between $|g\rangle$ and $|e\rangle$ oscillates in a sinusoidal manner at Rabi rate Ω (Figure 2-3). If all the cesium atoms are prepared in the ground state $|g\rangle$, the application of a Raman pulse for the duration of a half-cycle transfers atoms into the ground state $|e\rangle$; this pulse is often called π pulse. If the Raman pulse duration is a quarter-cycle, the atoms have equal probability of being in $|g\rangle$ and $|e\rangle$. This pulse is usually referred to as a $\pi/2$ pulse. A π pulse serves as an atom mirror, while a $\pi/2$ pulse works as an atom beamsplitter.
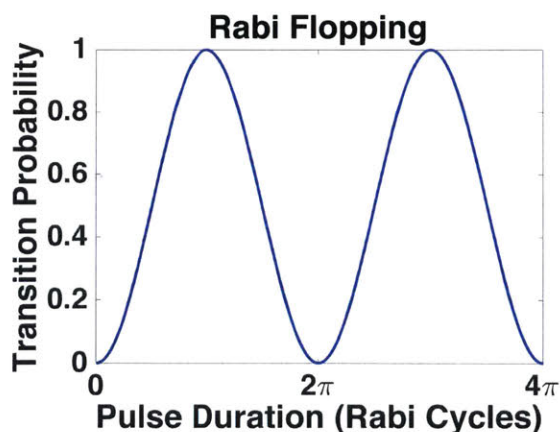
Figure 2-3: Schematic diagram of Rabi cycling (i.e., flopping). The probability of an atomic transition oscillates between $|g\rangle$ and $|e\rangle$ in a sinusoidal manner with increasing pulse duration.

The effective Rabi rate Ω_{eff} of a Raman transition is related to the single-photon Rabi rates Ω_1 and Ω_2, as well as single-photon detuning Δ, by the equation

$$\Omega_{eff} = \frac{\Omega_1 \Omega_2}{2\Delta} \tag{2.5}$$

where Ω_1 and Ω_2 are the complex Rabi rates of two Raman laser fields that couple the ground states to the excited state, respectively.

The Raman detuning δ (Figure 2-2) is a critical quantity in Raman timekeeping. It is equal to the difference in frequency between the atom transition frequency and the local oscillator being tuned to the atomic reference, so that atomic phase evolution during a measurement is proportional to δ. The detuning also affects the interaction of the Raman optical pulse with the atoms in producing the superposition of ground states. The application of Raman interferometry to atomic timekeeping will be discussed in Section 2.4.

One advantage of stimulated Raman transition for atomic timekeeping is the compact size of the apparatus when compared with microwave interrogation. The disadvantage is that the interaction between Raman lasers and cesium atoms can cause AC Stark shift (or light shift), which perturbs the energy of hyperfine ground states. However, the differential AC Stark shift can be cancelled or suppressed if the intensity ratio of two Raman lasers is adjusted properly [1, 11].

If the AC Stark shift of ground state $|g\rangle$ is Ω_g^{AC}, and the AC Stark shift of ground state $|e\rangle$ is Ω_e^{AC}, then the differential AC Stark shift δ_{AC} is

$$\delta_{AC} = \Omega_e^{AC} - \Omega_g^{AC} = \frac{\Omega_2^2 - \Omega_1^2}{4\Delta} \tag{2.6}$$

where $\Omega_e^{AC} = \frac{\Omega_2^2}{4\Delta}$; $\Omega_g^{AC} = \frac{\Omega_1^2}{4\Delta}$.

The differential AC Stark shift (δ_{AC}) is a function of the intensity ratio of two Raman lasers. For a fixed single-photon detuning Δ, the δ_{AC} value monotonically increases from negative to positive with the increase of intensity ratios. There is a desired ratio R_0 at which δ_{AC} is exactly zero.

Another possible approach to compensate for the differential AC Stark shift might

be to adjust the Raman detuning δ; however, this method is not viable. The AC Stark shift is proportional to the intensity of the applied field. Since the Raman beam has a Gaussian spatial intensity profile, the AC Stark shift of a particular atom depends on its location within the beam. Thus, application of a fixed Raman detuning to all the atoms cannot compensate for the Stark shift of the atoms as a whole. However, if the Raman beams are transmitted in the same optical fiber with constant intensity ratio, then suppression of AC Stark shift can be more effective and accurate. Further, Kotru et al. found that use of Adiabatic Rapid Passage (discussed in 2.3) suppresses phase sensitivity to AC Stark shifts [7].

2.2.1   General Analytical Theory

The mechanism of stimulated two-photon (Raman) transitions in cesium is described here. The following derivation closely follows [1]. The effect of spontaneous emission is excluded, since the natural linewidth is much less than the single-photon detuning $\Gamma \ll \Delta$.

The system comprises three levels, as shown on the right side of figure 2-2: two ground states $|g\rangle$ and $|e\rangle$, and an intermediate state $|i\rangle$. Two fields are applied to the atoms: one of frequency ω_1 nearly resonant with the transition between $|g\rangle$ and $|i\rangle$, and other of frequency ω_2 nearly resonant with the transition between $|e\rangle$ and $|i\rangle$. The energy origin is set to the average of $|g\rangle$ and $|e\rangle$, and the reference frame is that of the ground state $|g\rangle$. The Hamiltonian H for the three-level system then includes free and interaction parts

$$
\begin{aligned}
H &= H_A + H_I \\
&= \begin{bmatrix} \frac{\omega_{HFS}}{2} & 0 & 0 \\ 0 & \omega_i & 0 \\ 0 & 0 & \frac{\omega_{HFS}}{2} \end{bmatrix} + \begin{bmatrix} 0 & H_{I2} & 0 \\ H_{I2}^* & 0 & H_{I1}^* \\ 0 & H_{I1} & 0 \end{bmatrix}
\end{aligned}
\tag{2.7}
$$

where ω_i corresponds to the splitting between the energy origin and $|i\rangle$. The matrix elements of the interaction Hamiltonian are defined as

$$H_{I1} = \frac{\hbar}{2}|\Omega_1|e^{i\tilde{\phi}_1(t)} \tag{2.8a}$$

$$H_{I2} = \frac{\hbar}{2}|\Omega_2|e^{i\tilde{\phi}_2(t)} \tag{2.8b}$$

with $\Omega_1 = -q\langle g|\vec{\epsilon_1} \cdot \vec{r}|i\rangle$ and $\Omega_2 = -q\langle e|\vec{\epsilon_2} \cdot \vec{r}|i\rangle$ as the Rabi frequencies associated with ω_1 and ω_2, where ϵ_1 and ϵ_2 are the amplitudes of our applied fields. The phases $\tilde{\phi}_1$ and $\tilde{\phi}_2$ account for the applied field and momentum recoil from $\vec{k_{eff}} = \vec{k_1} - \vec{k_2}$:

$$\tilde{\phi}_1(t) = \int_0^t \left(\omega_1(t') - \vec{k_1} \cdot \dot{z}(t')\hat{z}\right) dt' + \phi_{1,0} - \vec{k_1} \cdot z(0)\hat{z} \tag{2.9a}$$

$$\tilde{\phi}_2(t) = \int_0^t \left(\omega_2(t') - \vec{k_2} \cdot \frac{\hbar\vec{k_{eff}}}{m} - \vec{k_2} \cdot \dot{z}(t')\hat{z}\right) dt' + \phi_{2,0} - \vec{k_2} \cdot z(0)\hat{z} \tag{2.9b}$$

The equations of motion arise from the Schrodinger equation, where we may substitute the expressions for the Hamiltonian:

$$i\hbar \begin{bmatrix} \dot{\Psi}_e \\ \dot{\Psi}_i \\ \dot{\Psi}_g \end{bmatrix} = H \begin{bmatrix} \Psi_e \\ \Psi_i \\ \Psi_g \end{bmatrix} \tag{2.10}$$

The Ψ_i may be eliminated by taking $\dot{\Psi}_i = 0$, which is reasonable provided $\Delta \gg \Omega_{eff}$. This simplifies the three level system to an effective two level system as also seen in [12].

$$\begin{bmatrix} \dot{c}_e(t) \\ \dot{c}_g(t) \end{bmatrix} = -\frac{i}{2}\vec{\Omega(t)} \cdot \vec{\sigma} \begin{bmatrix} c_e(t) \\ c_g(t) \end{bmatrix} \tag{2.11}$$

Where $\vec{\sigma}$ is the Pauli spin matrix operator $(\sigma_x, \sigma_y, \sigma_z)$, and the generalized Rabi rate is

$$\vec{\Omega} = \sqrt{\Omega_{eff}^2 + (\delta_{AC} - \delta')^2} \left(\cos\theta_j\hat{z} + \sin\theta_j(\cos\phi_j\hat{x} + \sin\theta_j\hat{y})\right) \tag{2.12}$$

with

$$\Omega_{eff} = \frac{\Omega_1 \Omega_2^*}{2\Delta} \tag{2.13}$$

$$\delta' = \omega_1(t) - \omega_2(t) - \left(\omega_{HFS} + \frac{\hbar k_{eff}^2}{2m} + \vec{k_{eff}} \cdot \dot{z}(t)\hat{z} \right) \tag{2.14}$$

$$\delta_{AC} = \frac{|\Omega_2|^2 + |\Omega_1|^2}{4\Delta} \tag{2.15}$$

The state vector is defined as

$$\Psi_\alpha(t) = e^{-\frac{i}{2}\delta_{AC}(t-t_j)} c_\alpha(t) \tag{2.16}$$

An atom starting in pure state $\vec{\Psi} = (0,1)$, where $|g\rangle = (0,1)$ and $|e\rangle = (1,0)$, evolves as follows

$$|\Psi(t)\rangle = \left[\cos\left(\frac{t\Omega}{2}\right) + i\frac{\delta_{AC} - \delta'}{\Omega} \sin\left(\frac{t\Omega}{2}\right) \right] |g\rangle - ie^{-i\phi} \frac{|\Omega_{eff}|}{\Omega} \sin\left(\frac{t\Omega}{2}\right) |e\rangle \tag{2.17}$$

where $\phi = \phi_{1,0} - \phi_{2,0} - \vec{k_{eff}} \cdot z(0)\hat{z}$.

For Raman resonant fields (i.e., $\delta_{AC} - \delta' = 0$, and $\Omega = \Omega_{eff}$), the above equation is simplified into

$$|\Psi(t)\rangle = \cos\left(\frac{t\Omega_{eff}}{2}\right) |g\rangle - ie^{-i\phi} \sin\left(\frac{t\Omega_{eff}}{2}\right) |e\rangle \tag{2.18}$$

Equations 2.17 and 2.18 show the sinusoidal oscillations characteristic of Rabi flopping.

2.2.2 Bloch Sphere Representation

As discussed earlier, the stimulated Raman transition with a large single-photon detuning Δ could be simplified into a two-level system, which can be intuitively visualized on the Bloch sphere. This is strongly suggested from the form of $\vec{\Omega}$ in

Equation 2.12, which represents the applied field driving the atomic transition. The polar angle θ is defined by

$$
\begin{aligned}
\cos\theta &= \frac{\delta_{eff}}{\Omega} \\
\sin\theta &= \frac{\Omega_{eff}}{\Omega}
\end{aligned}
\tag{2.19}
$$

where $\delta_{eff} = \delta_{AC} - \delta'$. The atomic state is represented as a pseudospin vector on the Bloch sphere by projecting the density matrix for ground states $|g\rangle$ and $|e\rangle$

$$
\rho(t) = |\Psi\rangle\langle\Psi|
\tag{2.20}
$$

onto Pauli spin matrices:

$$
\begin{aligned}
P_j(t) &= Tr[\rho(t) \cdot \sigma_j] \\
\vec{P}(t) = \begin{bmatrix} P_x \\ P_y \\ P_z \end{bmatrix} &= \begin{bmatrix} 2\Re[\rho_{eg}] \\ -2\Im[\rho_{eg}] \\ \rho_{ee} - \rho_{gg} \end{bmatrix}
\end{aligned}
\tag{2.21}
$$

These relationships may be visualized in Figure 2-4, where $\vec{P} = \hat{p}$ is a unit vector residing on the surface of the Bloch sphere. The equation of motion for this vector is

$$
\frac{\mathrm{d}}{\mathrm{d}t}\vec{P}(t) + \vec{P}(t) \times \vec{\Omega} = 0
\tag{2.22}
$$

The equation of motion is of the same form as that used in nuclear magnetic resonance, in which nuclear spin precesses around a magnetic field ($\sim$ Larmor precession).

With the above discussion, the action of a Raman pulse can be easily visualized on the Bloch sphere (Figure 2-5). The first scenario is of a resonant drive field (i.e., effective Raman detuning $\delta_{eff} = 0$, or $\theta = \pi/2$). Suppose an atom is prepared in state $|e\rangle$, so that atomic population vector $\hat{p}$ initially points straight up and is aligned with the positive z axis. The application of a resonant Raman pulse rotates $\hat{p}$ from the positive z axis to the positive x axis when the Raman pulse duration is $t = (\pi/2)/\Omega$

32
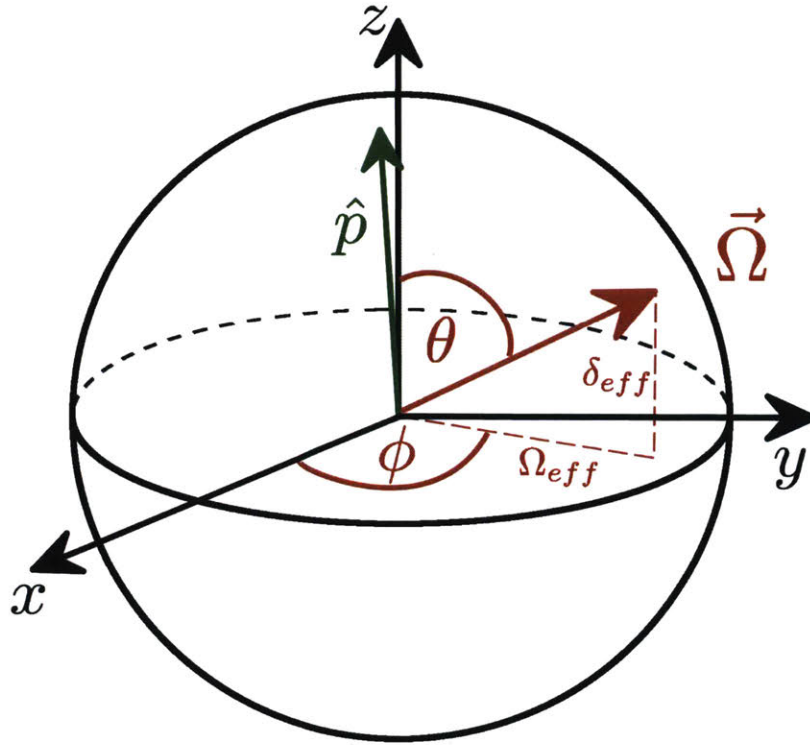
Figure 2-4: Bloch sphere representation of two-level system with $\hat{p}$ as pseudospin vector representing the atomic population and $\vec{\Omega}$ representing the applied field driving Raman transitions. θ and ϕ are the polar and azimuthal angles, respectively. δ_{eff} is the effective Raman detuning and Ω_{eff} is the effective Rabi rate. Vector $\hat{p}$ is a unit vector from the origin to the surface of the Bloch sphere; when it is (anti)parallel to the z-axis, the atomic population is in pure state $(|g\rangle)|e\rangle$. Otherwise, the atomic population is in a superposition of these states.

(a)   (b)
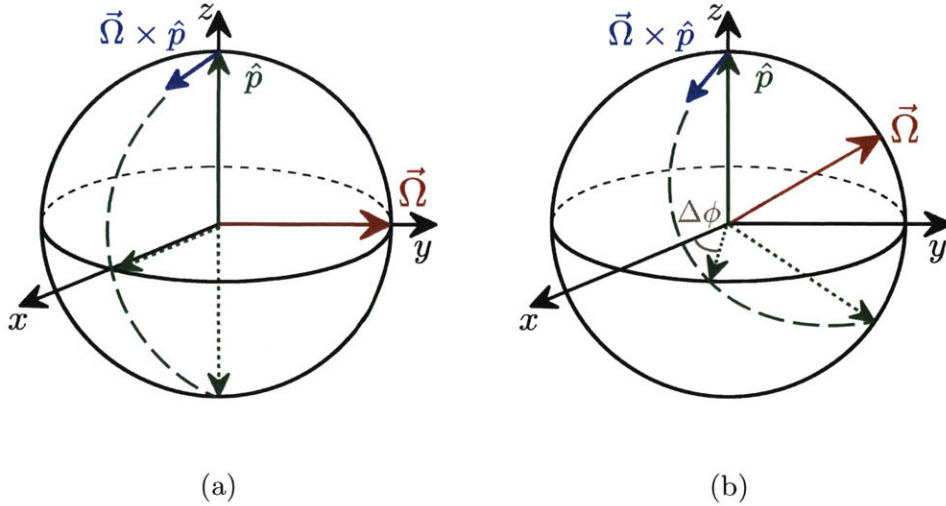
Figure 2-5: Rotation of atomic population vector $\hat{p}$ under Raman drive field $\vec{\Omega}$ on resonance (a) (i.e., effective Raman detuning $\delta_{eff} = 0$) and nearly resonant (b) with $\delta_{eff} \neq 0$. Detuning is exaggerated for clarity.

(a "$\pi/2$" pulse), or to the negative z axis when the Raman pulse duration is π/Ω (a "π" pulse), and so on. The pseudospin vector $\hat{p}$ rotates in a circular trajectory on the x-z plane as long as it is driven by Ω; i.e., it performs Rabi oscillations.

The second scenario is of a nearly resonant driving field with nonzero Raman detuning δ_{eff}, which is exaggerated for clarity in Figure 2-5. In contrast to the resonant Raman pulse, the drive field is slightly tilted away from y axis. The population vector rotates out of the x-z plane in a cone about the drive vector, and cannot exactly attain pure state $|g\rangle$ from starting state $|e\rangle$. In this case as well, $\hat{p}$ rotates at generalized Rabi rate $\Omega = \sqrt{\Omega_{eff}^2 + \delta_{eff}^2}$ about the drive field vector. The detuned $\pi/2$ pulse adds a systematic shift of atomic phase $\Delta\phi$, depicted between the Bloch vector and the x axis.

2.3   Raman Adiabatic Rapid Passage

As discussed previously, a resonant Raman π pulse flips an atom from ground state $|e\rangle$ exactly into $|g\rangle$. In reality, lasers are neither flawless nor monochromatic and their outputs vary in frequency and intensity. As a result, it is hard to produce a perfect resonant pulse. To circumvent these issues, a solution is the approach of

adiabatic passage, which slowly sweeps the Raman laser frequency across the atomic resonance (i.e., from off-resonance through resonance to off-resonance). The adiabatic passage π pulse efficiently transfers the atom between the ground state $|e\rangle$ and $|g\rangle$. The following discussion is closely based on the description in "Quantum and Atom Optics" [12].

"Dressed" states may be used to explain adiabatic passage. On a two-level atomic system with "bare" states $|g\rangle$ and $|e\rangle$, the phenomenon of Rabi flopping suggests that one may find new eigenstates that incorporate both the atom and the field. For clarity, this two-level atom with states $|g\rangle$ and $|e\rangle$ (with detuning δ) is used as an example. The free and interaction Hamiltonians in the rotating frame are

$$H = H_0 + H_I = \hbar \begin{bmatrix} -\delta & \frac{\Omega}{2} \\ \frac{\Omega}{2} & 0 \end{bmatrix} \tag{2.23}$$

where Ω is the Rabi rate. Using $H\Psi = E\Psi$, the eigenenergies $E_\pm$ and dressed eigenstates $|\pm\rangle$ are

$$E_\pm = -\frac{\hbar\delta}{2} \pm \frac{\hbar\sqrt{\Omega^2 + \delta^2}}{2} \tag{2.24}$$

$$\begin{bmatrix} + \\ - \end{bmatrix} = \begin{bmatrix} \cos\theta & \sin\theta \\ -\sin\theta & \cos\theta \end{bmatrix} \begin{bmatrix} g \\ e \end{bmatrix} \tag{2.25}$$

where $\theta \in [0, \pi/2)$ is defined as $\tan(2\theta) = -\frac{\Omega}{\delta}$.

As seen in Figure 2-6, eigenenergies of bare states $|g\rangle$ and $|e\rangle$ are 0 and $-\hbar\delta$, respectively, which means the two states are degenerate at $\delta = 0$. In contrast, the eigenenergies of the dressed states have a splitting of $\hbar\Omega$ at $\delta = 0$.

For a large detuning $-\delta$, the dressed state $|-\rangle$ is the equivalent of bare state $|g\rangle$. Slowly (adiabatically) sweeping the frequency past resonance guarantees the atom remains in dressed state $|-\rangle$ for the entire process. When the sweeping ends at large detuning $+\delta$, the dressed state $|-\rangle$ converges to bare state $|e\rangle$. Therefore, an adiabatic passage π pulse induces a transition from $|g\rangle$ to $|e\rangle$. Similarly, adiabatic passage may
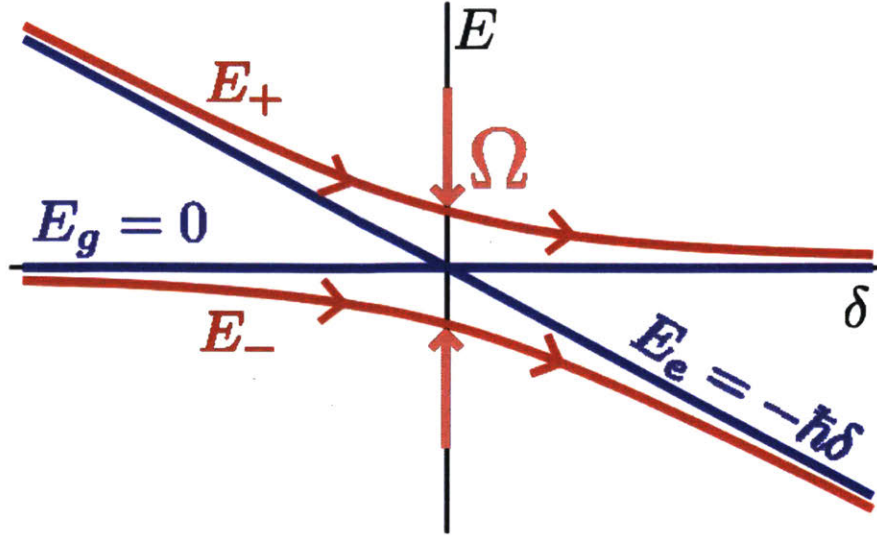
Figure 2-6: Energy levels of dressed states and bare states with avoided crossing. Red lines are the energy eigenvalues of dressed states $|+\rangle$ and $|-\rangle$. The blue lines indicate the energy eigenvalues of bare states $|g\rangle$ and $|e\rangle$. At very large detuning δ, the dressed states are approximately the same as the bare states, as indicated by the convergence of blue and red lines.

induce a transition from $|e\rangle$ to $|g\rangle$ by remaining in $|+\rangle$.

How slowly must the frequency change? The probability that an atom will tunnel to a different eigenstate can be calculated as

$$P_{tunnel} = e^{-\frac{\pi\Omega^2}{2|\partial_t\delta|}} \tag{2.26}$$

This implies that the adiabatic condition is

$$\Omega^2 \gg \left|\frac{\partial}{\partial t}\delta\right| \tag{2.27}$$

In this case, because the population vector precesses about the drive field vector at rate Ω, $\hat{p}$ circles $\vec{\Omega}$ much more quickly than the frequency changes. But, the frequency cannot be changed slower than the lifetime of the excited state. So, the change must be more "rapid" than this lifetime.

An adiabatic rapid passage π pulse can also be simply visualized on the Bloch sphere for a two-level system (Figure 2-7).

Assume that an atom begins in state $|e\rangle$ and thus the population vector is aligned
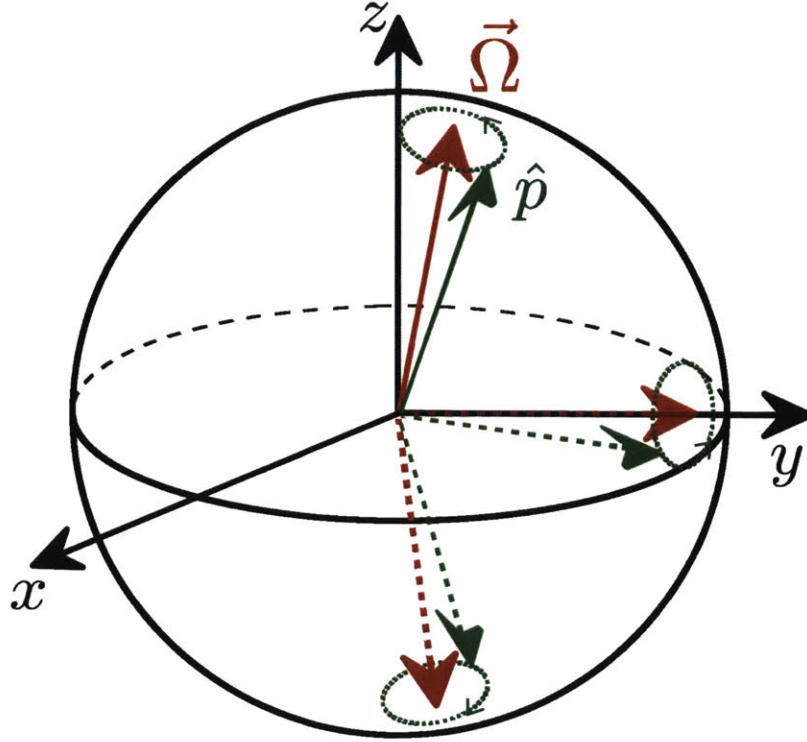
Figure 2-7: Rotation of population vector by a drive field Ω associated with Raman adiabatic passage. The Bloch vector $\hat{p}$ follows Ω under the adiabatic condition.

with the positive z axis. When the drive field $\vec{\Omega}$ is initially applied with a large detuning and thus small θ, $\hat{p}$ precesses rapidly about the drive field with little change in direction (about 2θ). When the drive field slowly moves under the adiabatic condition, Bloch vector $\hat{p}$ always adiabatically follows drive field $\vec{\Omega}$. Once the drive field reaches the negative z axis, the atom is in state $|g\rangle$.

There are several optimized adiabatic passage schemes. Raman ARP was developed recently by Draper Laboratory [7, 8] and was adopted in this thesis. Work by Kotru demonstrated that standard Raman pulses were about 75 times more sensitive to AC Stark shift as opposed to these ARP pulses (Figure 2-9), a significant result. Thus, ARP is the focus of this thesis. Raman ARP uses a combination of frequency and intensity modulations for efficient adiabatic transfer. A nonlinear sweep rapidly changes frequency and amplitude at the beginning as well as at the end of the ARP
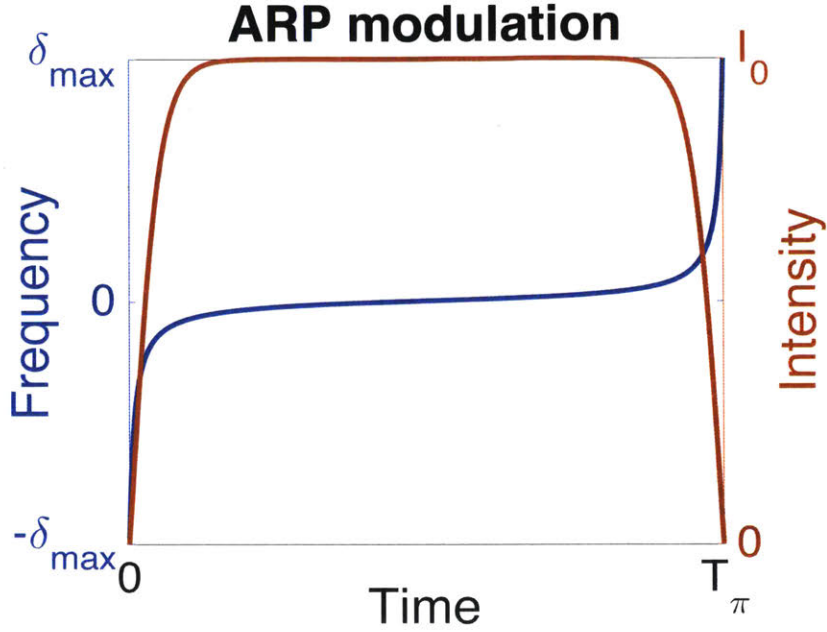
Figure 2-8: Frequency sweep and intensity modulation of Raman ARP, with rapid frequency chirps and low optical intensities at the beginning or the end of the pulse.

pulse (Figure 2-8). The ARP pulse chosen for this work has a frequency sqeep given by the equation

$$\delta(t) = \Omega_{arp} \tan\left[\alpha\left(\frac{2t}{T_\pi} - 1\right)\right] \quad , t \in [0, T_\pi] \tag{2.28}$$

where T_π is the total sweep duration, Ω_{arp} is the sweep rate, and $\alpha = \arctan(\delta_{max}/\Omega_{arp})$, where δ_{max} is the maximum detuning. This frequency sweep is simultaneously combined with an intensity modulation $I(t)$

$$I(t) = I_0 \tanh\left[\beta\left(1 - \left|\frac{2t}{T_\pi} - 1\right|\right)\right] \tag{2.29}$$

where I_0 is maximum intensity, and β is a parameter describing the extent of modulation deviation from a square shape.

Similar to the stimulated Raman pulses, Raman ARP also provides π (mirror) and $\pi/2$ (beamsplitter) pulses. An ARP π pulse starts with a large negative detuning, passes through resonance, and ends with a large positive detuning (Figure 2-8). An

38
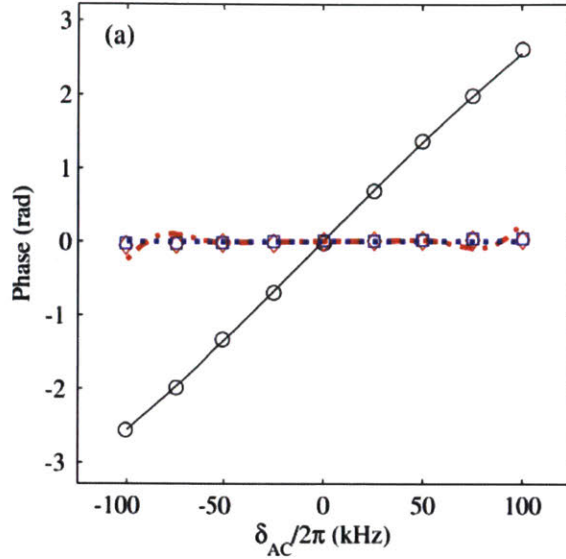
Figure 2-9: Clock phase shift data showing 75 times more sensitivity to AC Stark shift when using standard Raman as opposed to ARP. Black indicates standard Raman, red and blue indicate ARP with different frequency sweep times. Reproduced from [8].

ARP $\pi/2$ pulse can be the first half of the ARP π pulse, beginning with a large negative detuning and finishing on resonance. When the ARP $\pi/2$ pulse acts on a state of equal superposition, it is the equivalent of the second half of the ARP π pulse, from resonance to a large positive detuning.

2.4 Ramsey Interferometry and Atomic Timekeeping

Stimulated Raman and Raman ARP can drive the coherent population transfer between the two hyperfine ground states of cesium. In order to accurately compare the hyperfine frequency with that of the field, a long interaction time between the atom and field is required, as indicated by the time-frequency uncertainty [13]. The long interaction period entails many technical difficulties, creates enormous Stark shift, and may require a very large apparatus. However, Ramsey interferometry or Ramsey's method of separated oscillatory fields provides an excellent solution to this issue.

(a) First $\pi/2$ pulse   (b) Dwell time   (c) Second $\pi/2$ pulse
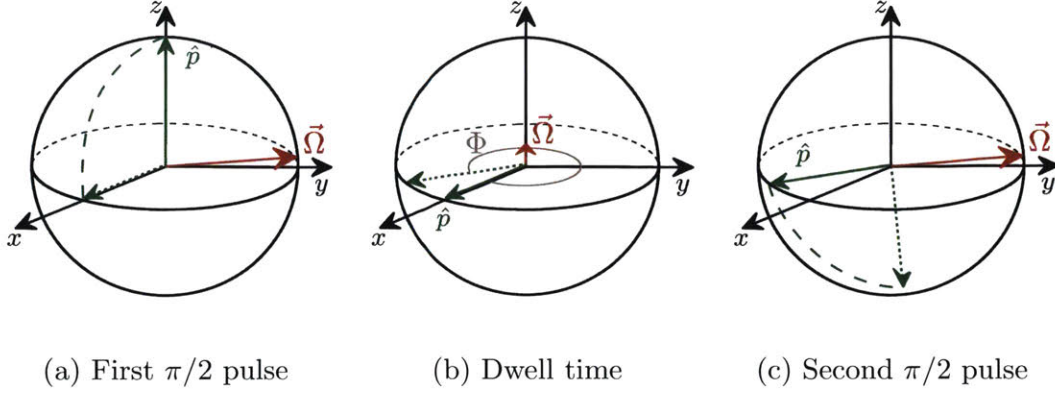
Figure 2-10: Two Raman $\pi/2$ pulses separated by a long dwell time. (a) In the first pulse, $\Omega \approx \Omega_{eff} \gg \delta$. (b) During the dwell time, the population vector rotates about the z-axis and accrues phase Φ due to preserved phase coherence with $\Omega = \delta$. (c) The second pulse is identical to the first, and rotates the population vector into a superposition of $|e\rangle$ and $|g\rangle$.

2.4.1 Ramsey Fringes

The idea of Ramsey's separated oscillatory fields is to apply laser or microwave field for a short time initially, followed by a relatively long dwell time with no applied field, and then the initial field again for a short time [14]. The beauty of this method is that phase coherence of the atoms is still preserved during the dwell time, thus equivalently increasing the interaction time. A Ramsey sequence is easily visualized on the Bloch sphere. Consider two Raman $\pi/2$ pulses separated by a long dwell time (Figure 2-10), with the frequency of the drive field very close to the atomic resonance ($\Omega \approx \Omega_{eff}$ or $\delta \ll \Omega_{eff}$). Assume the atom starts in the ground state $|e\rangle$ and the population vector is thus aligned with the positive z axis. The first $\pi/2$ pulse rotates the population vector nearly to the x-y plane. During the dwell time, the phase Φ accrues due to the small remaining detuning, and the differential AC Stark shift is zero because the Raman fields are off.

If Φ is an even-integer multiple of π after the dwell time, then the second $\pi/2$ pulse flips the atomic vector to the state $|g\rangle$. If the Φ is an odd-integer multiple of π after the dwell time, then the second $\pi/2$ pulse returns the atom to its initial state $|e\rangle$. For other Φ, the second $\pi/2$ pulse rotates the population vector into a superposition of $|e\rangle$ and $|g\rangle$, and the transition probability from $|e\rangle$ to $|g\rangle$ varies in a sinusoidally

with Φ. This sinusoidal relation is called Ramsey fringes or interferogram.

The phase Φ is determined by Raman detuning δ and the duration of dwell time T. During the dwell time, the population vector is rotating around the z axis at rate δ, and the accumulated phase is

$$\Phi = \delta T \tag{2.30}$$

If the Raman field is on resonance ($\delta = 0$), equation 2.30 shows that Φ is zero, and the two-pulse Ramsey sequence is equivalent to that of $\Phi = 2n\pi, n \in \mathbb{Z}$. The first $\pi/2$ pulse rotates the population vector to the x-y plane from the initial state $|e\rangle$, and the second $\pi/2$ pulse torques the atom to the state $|g\rangle$ from the x-y plane.
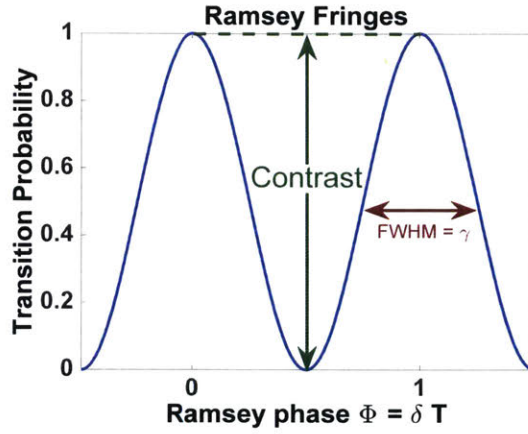
Figure 2-11: Ramsey fringes, showing the transition probability of an atom initiallly prepared in $|e\rangle$ defined as $\frac{P_g}{P_e + P_g}$. The transition probability varies in a sinusoidal manner due to the shifts of phase Φ. The full width half maximum (FWHM) of these fringes is the linewidth γ. Contrast is defined as the peak-to-trough distance.

Ramsey fringes can be obtained by varying δ or T. When the dwell time T is constant, the shifts in Raman detuning change the phase Φ and correspondingly the transition probability of ground state $|e\rangle$ as well (Figure 2-11).

The transition probability varies between 0 and 1, and can be written as $P_e = \cos^2\left(\frac{\Phi}{2}\right) = \frac{1}{2} + \frac{\cos\Phi}{2}$. Experimentally, taking into account contrast C and background B, the transition probability can be expressed as

$$P_e = \frac{1}{2} + \frac{C}{2}\cos\Phi + B \tag{2.31}$$

Additionally, the phase sensitivity to population change (or vice versa) may be determined by taking the derivative $d\Phi/dP$

$$\frac{d\Phi}{dP} = \frac{2}{C\sqrt{1 - \frac{(-2B+2P-1)^2}{C^2}}}$$ (2.32)

Assuming B = 0 and P = 0.5, we get

$$d\Phi = \frac{2}{C}dP$$ (2.33)

The linewidth of the Ramsey fringe is determined by the interrogation time (i.e., dwell time). It is defined as the full width half maximum and is shown in Figure 2-11. The relation between linewidth γ and Ramsey interrogation time T is through

$$\gamma = \frac{1}{2T}$$ (2.34)

A longer interrogation time results in narrower linewidth, and vice versa. For instance, the fringe linewidth is 50 Hz for a short interrogation time of 10 ms, and is improved to 1 Hz for a longer interrogation time of 500 ms. A narrower linewidth is desired to more precisely match the applied Raman field to the hyperfine splitting frequency. Cesium fountain clocks use long interrogation times facilitated by a tall cavity in which the atoms are thrown upwards and fall back down during the interrogation time. However, this cavity is large, e.g., about 1.5 meters tall in the NIST-F2 fountain clock [3]. For compact atomic timekeeping, short interrogation times are used at the expense of some accuracy.

2.4.2 Atomic Timekeeping

Atomic timekeeping in this thesis uses a simple two-pulse Ramsey sequence (i.e., $\pi/2 - \pi/2$) as discussed in section 2.4.1. The pulses are either stimulated Raman pulses or Raman ARP pulses. Both Raman beams are co-propagating (Figure 2-12), and the atom receives a negligible momentum kick after absorbing k_1 photon and emitting k_2 photon.
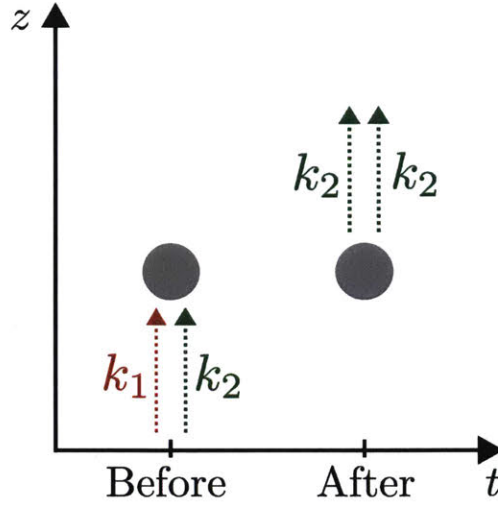
Figure 2-12: Co-propagating Raman beams with wavevectors $\vec{k_1}$ and $\vec{k_2}$ give the atom a very small momentum kick, which still imposes a limit on interrogation time but is about five orders of magnitude less than if the beams were counter-propagating and is thus negligible [1].

$$\hbar \left| \vec{k_{eff}} \right| = \hbar \left(\left| \vec{k_1} \right| - \left| \vec{k_2} \right| \right) \approx 0 \tag{2.35}$$

Operation of the interferometer for timekeeping is set at the midpoint of the interference fringe, called the "$\pi/2$" point. This point (Figure 2-13) has the steepest slope, and is thus most sensitive to phase fluctuations. That is, if the phase shifts slightly in either direction, the atoms will report this shift by a corresponding change in transition probability. Comparatively, operation at resonance or $\Phi = n\pi, n \in \mathbb{Z}$, where slope is zero, yields the least sensitivity to phase shift.

2.5   Atomic Accelerometer

An atomic accelerometer uses two counter-propagating Raman beams (Figure 2-14) to manipulate the quantum state of the atoms. These beams impart a total momentum kick of $\sim 2\hbar k_1$ to the atom after absorbing a k_1 photon and emitting a k_2 photon.
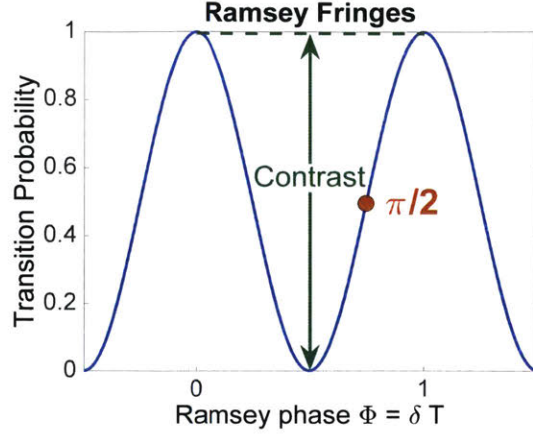
Figure 2-13: The midpoint of the fringe ("$\pi/2$") is most sensitive to shifts in phase $\Phi = \delta T$. Raman lasers are slightly detuned to such a δ value that keeps the transition probability at 0.5, while dwell time T is constant.

$$\hbar \vec{k}_{eff} = \hbar \left| \vec{k_1} \right| + \left| \vec{k_2} \right| \approx 2\hbar \left| \vec{k_1} \right| \tag{2.36}$$

An atomic accelerometer may be realized with a Mach-Zehnder three-pulse sequence $\pi/2 - \pi - \pi/2$. First, the atom trajectory is analyzed for the case of no acceleration (Figure 2-15 top). The cesium atoms are initially prepared in ground state $|g, p = 0\rangle$. The first $\pi/2$ beamsplitter pulse divides the atom wavepackets in two arms: the lower arm remains the original state $|g, 0\rangle$, whereas the upper arm experiences a state transition and momentum change $|e, 2\hbar k_1\rangle$. The two arms are spatially separated due to this momentum change. A subsequent π pulse deflects the two wavepackets back toward each other, acting as a mirror to change the lower arm into $|e, 2\hbar k_1\rangle$ and upper arm into $|g, 0\rangle$. The final $\pi/2$ pulse combines the wavepackets to create interference, after which detection of ground state and excited state populations may occur.

In the case of downward acceleration, the atom trajectory is different from that of no acceleration (Figure 2-15 bottom).

The phase shift between the upper and lower arms is expressed as [15, 16]

$$\Delta\phi = \phi_{upper} - \phi_{lower} = \tilde{\phi}_{2T} - 2\tilde{\phi}_T + \tilde{\phi}_0 \tag{2.37}$$

44
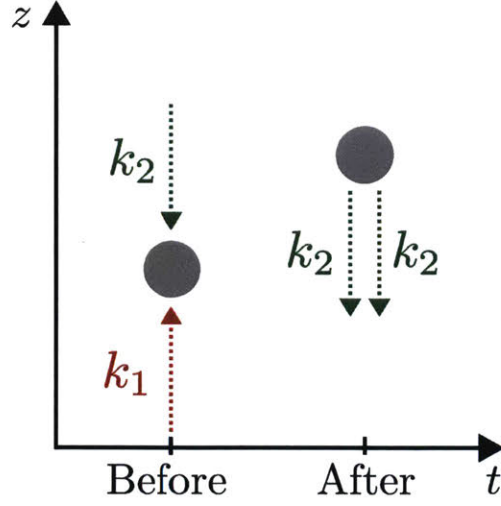
Figure 2-14: Counter-propagating Raman beams with wavevectors k_1 and k_2 give the atom a momentum kick of $\hbar \left| \vec{k_1} \right| + \left| \vec{k_2} \right| \approx 2\hbar \left| \vec{k_1} \right|$.

Where $\tilde{\phi}$ is the Raman-imprinted phase on atoms, which is equal to the phase difference between the two Raman beams. Subscripts 2T, T and 0 indicate the time of Raman pulse.

The above phase shift due to the three pulses can also be written as

$$\Delta\phi_{light} = \phi_0 - \phi_{upper,T} - \phi_{lower,T} + \phi_{2T} \tag{2.38}$$

The relationship between the acceleration and the phase shift $\Delta\phi$ is as follows

$$a = \frac{\Delta\phi}{k_{eff}T^2} \tag{2.39}$$

Note the scale factor for the acceleration is $|k_{eff}|T^2$, implying that precision can be enhanced by either transferring more momentum to the atoms or increasing the interrogation time.

45
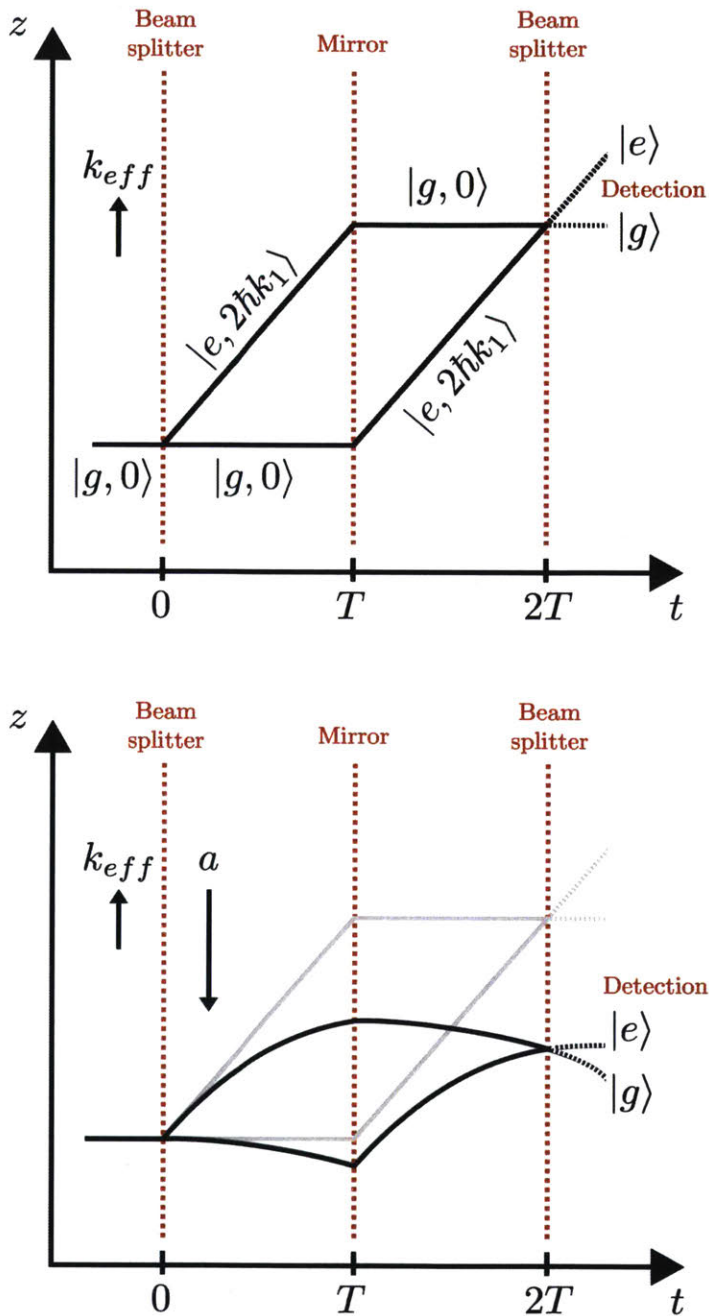
Figure 2-15: Atom interferometer set up with $\pi/2 - \pi - \pi/2$ pulse sequence. X-axis displays time, while y-axis displays position. The top graph shows an interferometer under no acceleration, with atom trajectory and state $|E, p\rangle$ in black. Red dotted lines denote applied Raman pulses, which act as atom optics in the interferometer to split, reflect, and recombine the wavepackets for eventual state detection. The bottom diagram shows the same interferometer under acceleration in black, with non-accelerated atom trajectory in gray for comparison.

Chapter 3

Apparatus

3.1 Vacuum System

Atom interferometry requires a long coherence time (up to 1000 ms) to achieve high sensitivity. Collisions between the cesium and other background atoms may lead to spurious phase shifts in the interferometer and should be avoided. Therefore, ultra-high vacuum is needed to perform Ramsey interferometry. The vacuum cell used (about 80 cm^3) is made of quartz in an octagonal shape (Figure 3-1), with seven 1-inch and two 2.3-inch diameter optical flats as windows permitting light beams to enter the cell. The quartz cell is initially vacuumed using a turbo pump and baked at 150°C. Then, getter and ion pumps are switched on while the turbo pump is switched off. These pumps are attached to the cell by metal flanges. The getter pump removes non-noble gases; the ion pump eliminates helium that permeates quartz. Eventually a vacuum of $\sim 10^{-9}$ Torr is achieved and maintained in the cell.

The shape of the quartz cell allows for excellent laser access, including magneto-optical trap (MOT), Raman, pushing, and state preparation beams (Figure 3-2). The large 2.3-inch windows also enable the fluorescence detector to be placed closer to the atoms.

Cesium atoms in the quartz cell are sourced by a current-driven metal dispenser, which is placed in the neck of the cell, so that cesium vapor may enter the center of the cell which is the trap region.
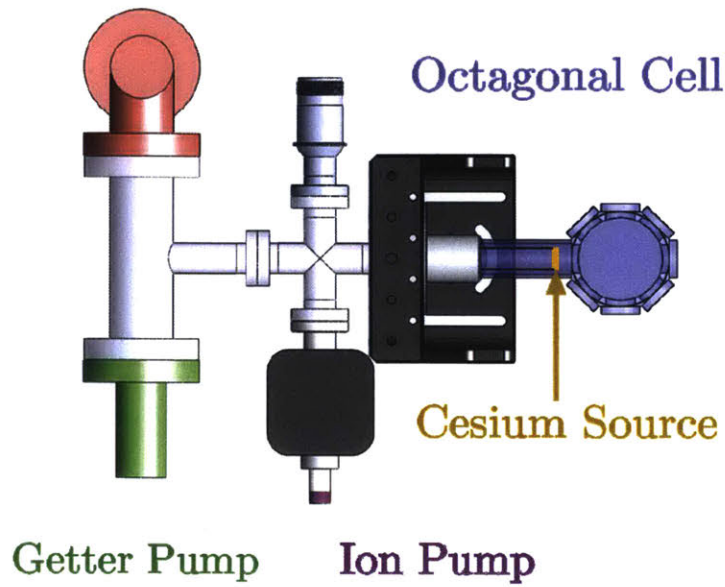
Figure 3-1: Configuration of quartz vacuum cell, turbo pump, getter pump and ion pump. Cesium source can be seen inside cell neck.
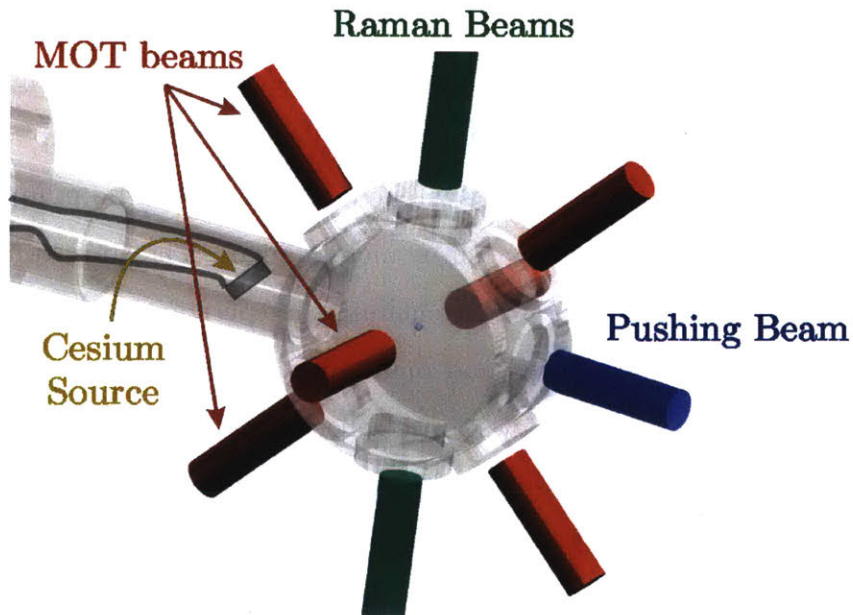

Figure 3-2: The octagonal shape of the quartz vacuum cell allows easy placement of magneto-optical trap (MOT), Raman, and pushing beams. Cesium source is visible inside the cell neck.

3.2 Magneto-Optical Trap

Laser cooling and trapping of atoms [17, 18] are critical to atomic timekeeping. Cooling can significantly reduce the kinetic energy of atoms, which goes as $mv^2/2$. At room temperature, cesium atoms move on the order of ~ 100 m/s. After they are cooled down to a few microKelvins, their velocity is reduced to the order of ~ 1 cm/s. Laser trapping is capable of confining cesium atoms into a small volume at sufficiently high density for interrogation. A combination of both techniques allows for longer interrogation times via Ramsey interferometry for high sensitivity, and significantly reduces the Doppler effect for fast-moving atoms.

Laser cooling is largely based on two principles: The Doppler effect and momentum conservation. Consider a laser beam tuned slightly below the atomic resonance frequency. The atoms moving along the laser propagation direction will see a frequency farther below resonance, and absorption is less likely to occur. The atoms moving against the laser propagation direction will see a frequency closer to resonance, making them more likely to absorb photons. When the atom absorbs a photon, the excited atom receives a momentum transfer in the direction of laser propagation and then emits a photon in a random direction (Figure 3-3). After absorbing numerous photons, the atom gains sufficient momentum in the direction opposite its initial velocity and slows. The slower atom will see a laser frequency farther from resonance, making it less likely to absorb more photons. The recoil momentum from emission of photons in random directions will average to zero. This effect is known as "optical molasses".

Laser trapping is based on the Zeeman Effect and is realized by the application of an inhomogeneous magnetic field. A one-dimensional trap is shown in Figure 3-4. Two anti-Helmholtz magnetic coils are placed on each side of atoms, creating a magnetic field that changes linearly with a minimum in the center, negative magnetic values on left and positive magnetic values on right. The corresponding Zeeman splitting induced in the atoms will be position-dependent; those at the center will have no Zeeman splitting whereas the atoms away from the center have a larger

49
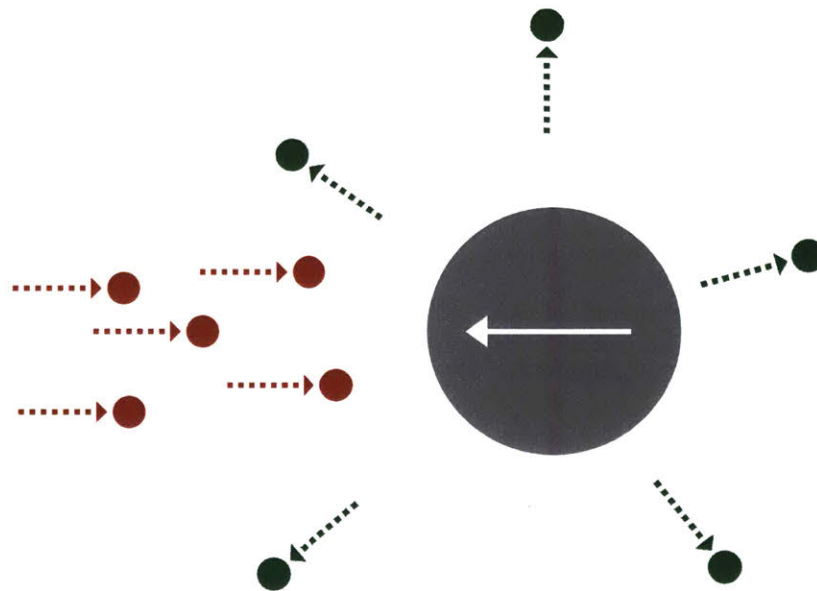
Figure 3-3: An atom (gray) has velocity in the direction opposite to that of incoming photons (red), which are tuned slightly below resonant frequency. Due to the Doppler effect, the atom sees incoming photons as resonant. These photons excite and impart momentum in their travel direction on the atom when absorbed. The atom then emits photons (green) in random directions, its velocity decreasing.
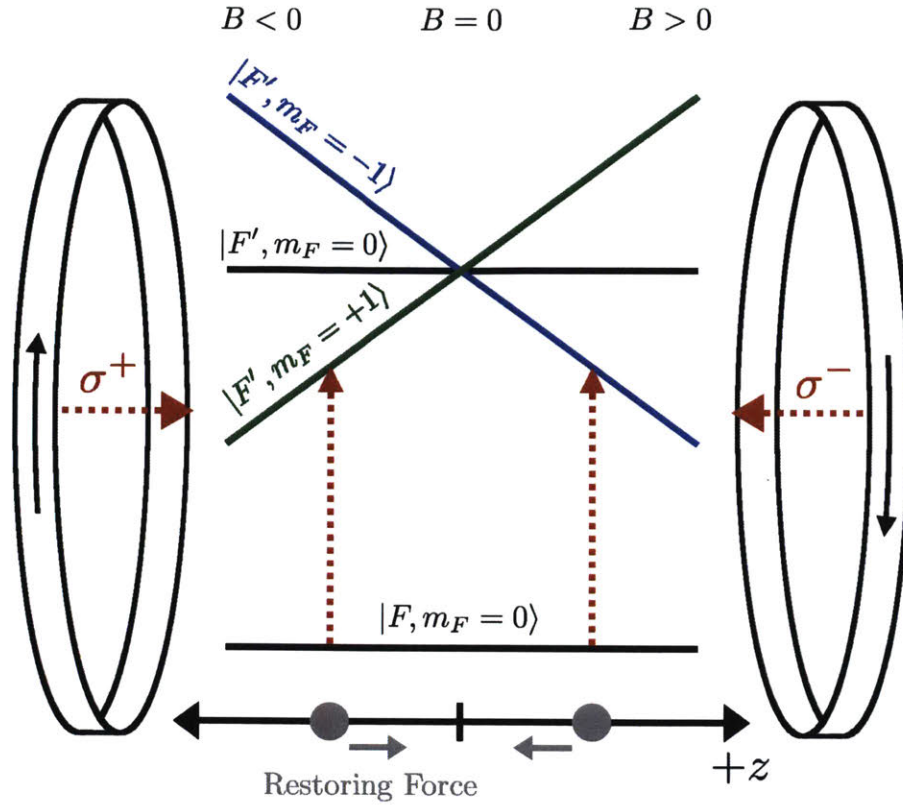
Figure 3-4: A one-dimensional magneto-optical trap (MOT) consists of anti-Helmholtz magnetic coils with two circularly polarized laser beams (σ^+, σ^-). F indicates ground state, and F' excited state. Zeeman splitting of magnetically sensitive states $(m_F = -1; m_F = 0; m_F = +1)$ increases away from the z = 0. Gray dots represent atoms, with gray arrows showing directions of the restoring force caused by the MOT. B is the magnetic field produced by the anti-Helmholtz magnetic coils.

splitting between magnetically sensitive states $m_F = -1, 0, +1$. Note $m_F = +1$ has the lowest energy on left side, whereas $m_F = -1$ has the lowest energy on right side.

Two circularly polarized laser beams (σ^+, σ^-) are counter-propagated and tuned slightly below the zero field atomic resonance. The σ^- photons induce transition to the $m_F = -1$ state, and similarly with σ^+ photons and the $m_F = +1$ state. Therefore, the left-propagating photons are closer to resonance with the $|F, m_F = 0\rangle \rightarrow |F', m_F = -1\rangle$ transition on the $z > 0$ side but far below it on the $z < 0$ side. So, atoms at $z > 0$ are more likely to absorb σ^- photons and gain momentum
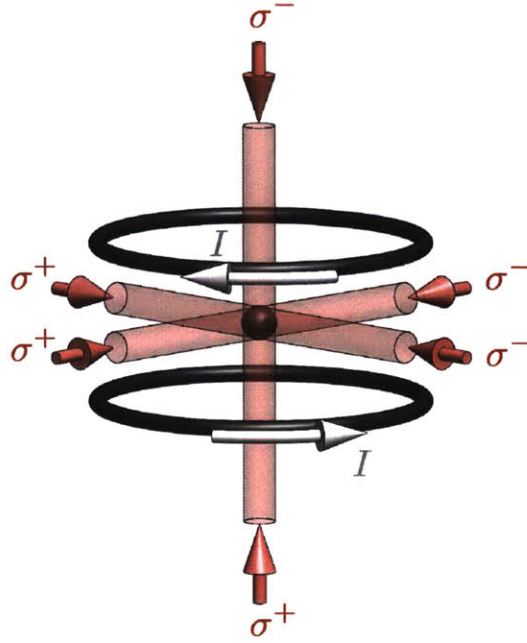
Figure 3-5: A three-dimensional magneto-optical trap consists of an anti-Helmholtz coil pair along the z-axis with opposing circularly polarized laser beams σ^+ and σ^- along each of the three orthogonal directions.

towards the origin. Similarly, the σ^+ photons are closer to resonance with $|F, m_F = 0\rangle \to |F', m_F = +1\rangle$ for $z < 0$ and will push the atoms rightwards toward the origin.

In three dimensions, there are instead three pairs of circularly polarized laser beams counter-propagating along three orthogonal axes. These are tuned to drive the cesium atoms cyclically between F = 4 and F' = 5. Atoms initially in F = 3 are moved to F = 4 via a "repump" beam (details in section 3.3) so that they too may be trapped. The anti-Helmholtz magnetic coils are placed along the z-axis (Figure 3-5), creating a quadrupolar magnetic field with minimum magnitude of zero at the center of the MOT [17]. Usually, $10^5 - 10^7$ atoms are trapped and cooled to $\sim 20\mu K$ in about 500-600ms.

3.3 Optical System

Three Toptica laser systems are used to provide cooling/trapping, state preparation, readout, repump and Raman beams. Toptica generates a laser beam of frequency
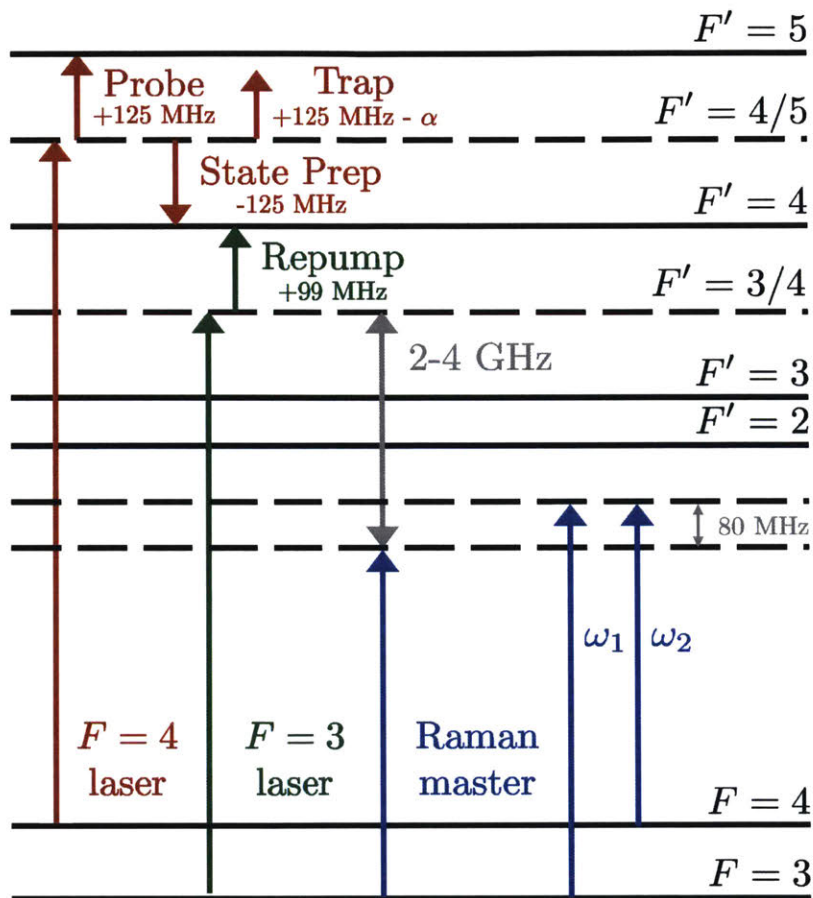
Figure 3-6: Laser frequencies used are shown on the Cesium D_2 hyperfine structure. Probe, trapping, and state prep beams are generated from an F = 4 to 4/5 cross laser (red), repump frequency is generated from an F = 3 to 3/4 cross laser (green) and Raman frequencies are generated from a Raman master offset-locked to F = 3 to 3/4 cross (blue). This diagram is not drawn to scale.

852nm (352 THz), which is roughly equal to the cesium D_2 transition from ground states to excited states. With acousto-optic modulators (AOMs), the laser beams are finely modulated on the order of MHz to satisfy the requirements of different transitions such as $F = 3 \rightarrow F' = 4$ or $F = 4 \rightarrow F' = 5$. These AOMs are controlled with a LabVIEW program that can adjust their frequency and turn them on/off with precise timing. The cooling/trapping, state preparation, readout, repump and Raman beams are illustrated in Figure 3-6 in the context of the cesium atom hyperfine structure.

The first Toptica unit (F = 4 laser system) is locked by saturation absorption spectroscopy [19] to the $F = 4 \rightarrow F' = 4/5$ crossover frequency, mainly providing cooling, readout and state prep lasers. The readout laser is offset +125 MHz from this locked frequency, and the cooling laser is offset by +125 MHz - α where $\alpha \approx 2\Gamma$ is 10-15 MHz; the cesium state prep laser is offset -125 MHz from this locked frequency (Figure 3-6). The second Toptica (F = 3 laser system) is locked to the $F = 3 \rightarrow F' = 3/4$ crossover frequency, providing a repump laser frequency which is offset +99 MHz from it. The third Toptica is for Raman laser generation, and the Raman Master laser is detuned 2 to 4 GHz from the F' = 3/4 crossover frequency.

The optics of the F = 4 laser system are shown in Figure 3-7, and is composed mainly of acousto-optic modulators (AOM), wave plates, polarizing beam splitter (PBS) cubes, tapered diode amplifiers (TA), and collimators.

An AOM modulates frequencies at MHz scale, and also works as a very fast shutter switching off in about 10-100 ns. The input light frequency can be shifted up or down as desired, e.g., +125 MHz or -125 MHz. An AOM can be single passed or double passed, shifting the frequency once or twice.

A combination of polarizing beam splitters and half-wave plates is used to tune the linear polarization of the light. Quarter wave plates turn plane-polarized light into circularly polarized light, and vice-versa. Used with a mirror, it will make sure the reflected light has orthogonal polarization to incident light. A PBS may then be used to direct the reflected light in a direction orthogonal to the incoming light.

The light from the F = 4 laser starts from the Toptica Pro tunable diode laser
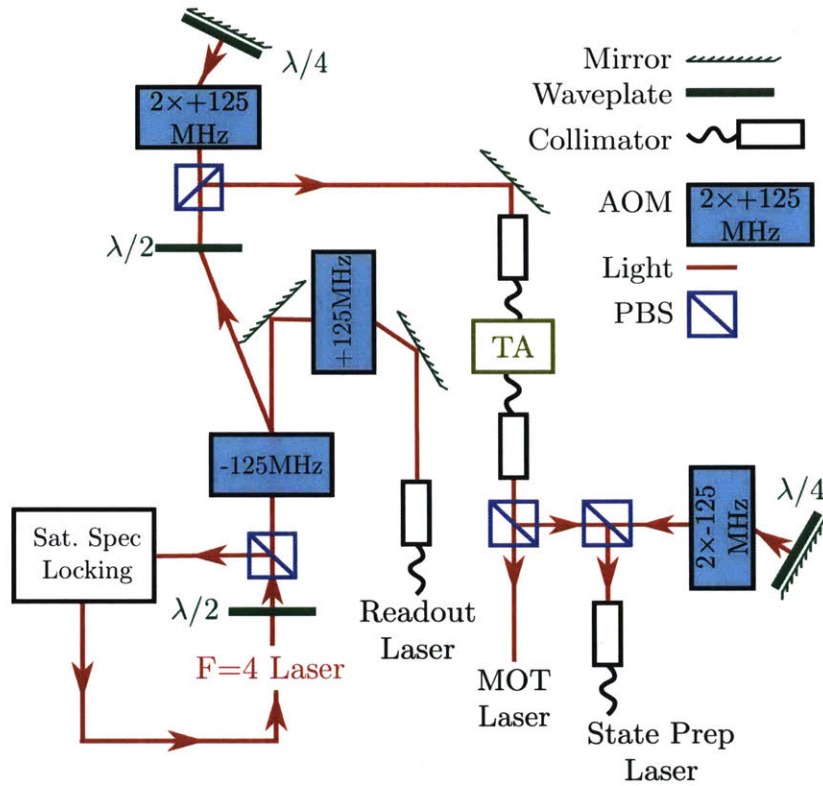
Figure 3-7: Diagram of F = 4 laser used for atom cooling/trapping, state preparation, and readout of atom population. This is a simplified form of the actual optical setup which excludes extraneous components due to real-life spatial constraints (e.g., mirrors and optical fibers).
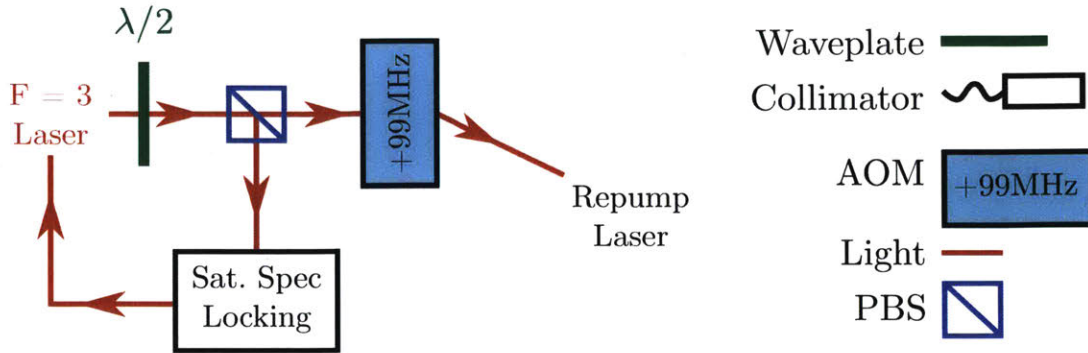
Figure 3-8: Diagram of F = 3 laser optics used to generate light for repump laser.

unit, and passes through a half wave-plate ($\lambda/2$) to control the polarization such that a small amount of the light goes to locking the laser frequency to the F = 4 → F' = 4/5 crossover by saturated absorption spectroscopy. The rest of the light passes through an AOM that shifts some of the light by -125 MHz. The unmodulated light goes through another AOM with a frequency modulation of +125 MHz, and is used for the readout (probe) laser. The modulated light double passes another AOM where its frequency is modulated twice by +125 MHz (+250 MHz in total). This light is amplified with a tapered amplifier (TA) from 8 mW to 100 mW of optical power. Ninety percent of this laser is used for cooling/trapping, and will be combined with repump light from the F = 3 board to be delivered to the atoms. The other 10% double passes an AOM with a frequency shift of -250 MHz and becomes cesium state prep light.

The optics of F = 3 laser system is shown in Figure 3-8. The F = 3 Toptica Pro laser is similarly locked to the F=3 → F'=3/4 crossover frequency. The light then passes through an AOM that shifts the light by +99 MHz. This laser becomes repump light, and is combined with cooling/trapping light from the F = 4 board to be delivered to the atoms.

Raman light is generated by another Toptica Pro laser (Figure 3-9). To reduce spontaneous emission, the Raman master light at frequency ω_{RM} is first detuned by

56
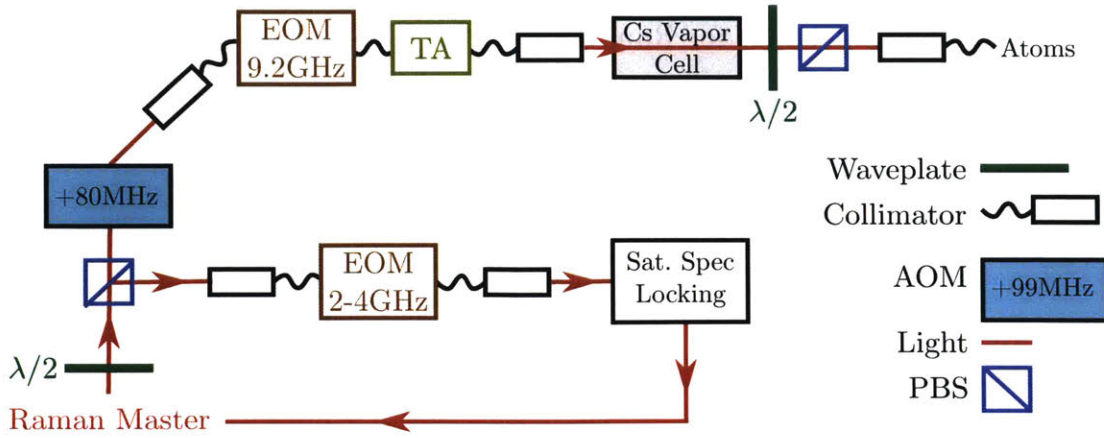
Figure 3-9: Diagram of Raman laser optics used to generate the two Raman frequencies. The Raman laser is offset locked to $-\Delta = 2\text{-}4$ GHz from resonance.

$-\Delta = 2$ to 4 GHz using an electro-optic modulator. This detuned light is adjusted to the F=3 → F'=3/4 crossover frequency $\omega_{3-3/4}$ via saturated absorption spectroscopy, which then locks the Raman laser to output light at this fixed detuning $\omega_{RM} = \omega_{3-3/4} + \Delta$ as seen in Figure 3-6. The Raman laser light then passes through a +80 MHz AOM which acts as a fast shutter.

To generate a pair of lasers for stimulated Raman transition, the Raman master light is passed through another EOM, which creates ±sidebands (Figure 3-10) that are spaced from the Raman master frequency by 9.2 GHz (i.e., ω_{HFS}). A tapered amplifier (TA) follows the second EOM and increases the Raman optical power to 40 mW. Then, the light passes through a cesium vapor cell to minimize amplified spontaneous emission due to the TA, before it is polarized and sent to the atoms.

Theoretically, any two lasers that are spaced by ω_{HFS} are able to stimulate a Raman transition; however, the carrier (ω_{RM}) and -1 sideband frequencies are chosen as the Raman pair, which drive the dominant Raman transition. The other frequency pair pictured, Raman Master and +1 sideband, generates much weaker Raman transitions due to its large frequency offsets from the F = 3 D_2 transitions and F = 4 D_2 transitions.

Similarly to the Zeeman effect with magnetic fields, an applied electric field causes shifts in the energy levels of cesium. This is called the Stark shift. The Raman lasers
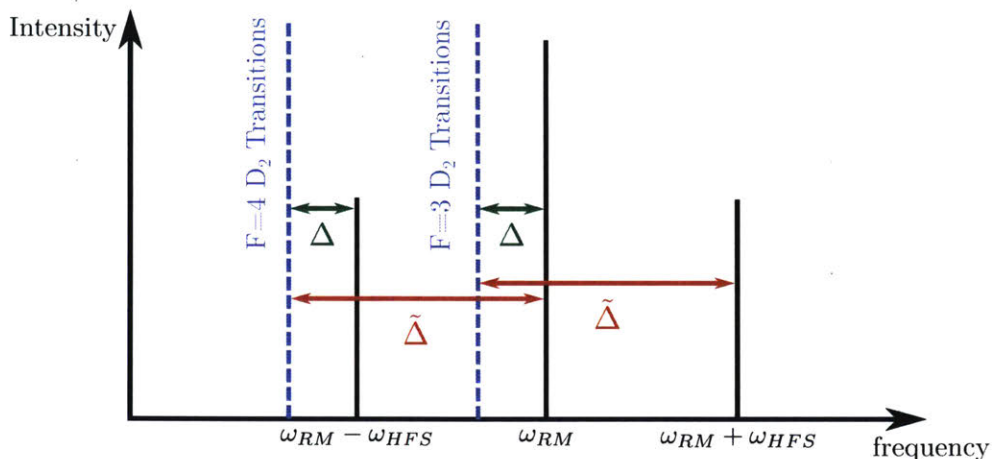
Figure 3-10: The spectrum of frequencies generated by the second Raman EOM is shown in black. The -1 sideband and carrier frequency are both detuned by Δ (green) from the $|4\rangle$ and $|3\rangle$ transitions to $|i\rangle$ which is the 3/4 crossover frequency in this case. It is also possible to use the +1 sideband and carrier frequency to generate Raman transitions, with detuning $\tilde{\Delta}$ (red). Because the detuning is larger, this Raman transition is weaker.

apply an oscillating electric field because they are electromagnetic waves, inducing a so-called AC Stark shift, discussed in 2.2. Due to the different intensities of the two Raman lasers, they each induce their own AC Stark shift in the two ground states of cesium. This differential AC Stark shift between the two lasers perturbs the hyperfine frequency ω_{HFS}.

The accuracy of timekeeping with cesium depends on the constancy of the hyperfine frequency. Thus, in experiments, it is desirable to adjust the intensity ratio of the two Raman lasers so that they each induce the same AC Stark shift in the F = 3 and F = 4 states and ω_{HFS} remains constant.

The phase-shifting and Raman frequency sweeping are controlled by the microwave signals that drive the EOM. Figure 3-11 provides a simplified diagram of the RF circuitry for Raman EOM and AOM signals. A single-sideband mixer (Polyphase Microwave SSB90110A) combines the dynamic 30 MHz signal from the AWG (Agilent N8241A) with a constant 9.163 GHz signal (Agilent E8257D). The Raman laser
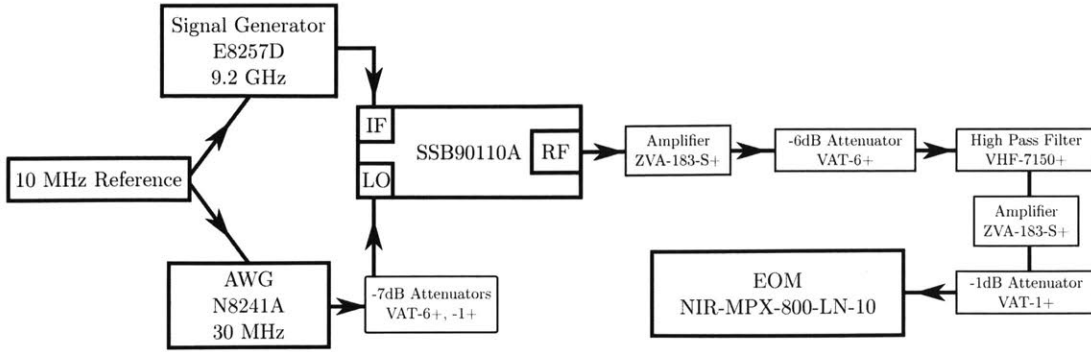
Figure 3-11: Block diagram of radio frequency (RF) circuit used to generate the 9.2 GHz frequency for the Raman EOM. Attenuators, amplifiers, and high pass filter ensure the output is power- and frequency-appropriate.

frequency difference is given by

$$|\omega_1 - \omega_2| = \nu_{E8257D} + \nu_{N8241A}(t) \tag{3.1}$$

Interferograms are generated by scanning the relative phase between the two lasers. The transition probability at each phase is measured multiple times and averaged.

3.4 Cesium Ground State Preparation

The cold cesium atoms are prepared in a ground state of $|F = 3, m_F = 0\rangle$ before Raman beams are applied to them. Atoms are sensitive to spatially and temporally-varying magnetic fields, as seen when they are trapped. To reduce interferometer sensitivity to spurious magnetic fields, the atoms are prepared in $m_F = 0$.

State preparation starts with the application of a magnetic bias field created by two Helmholtz coils (Figure 3-12). Then linearly polarized light resonant with the F = 4 → F' = 4 transition, called "state prep" light (Figure 3-6), is applied along the magnetic field axis to optically pump the atoms into a magnetically insensitive state. Repump light was simultaneously applied to excite F = 3 atoms to F' = 4, preventing accumulation of atoms in the F = 3 hyperfine ground state. This process transfers
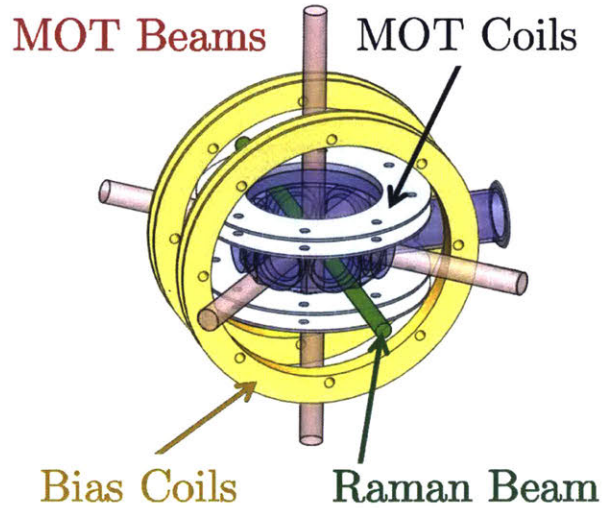
Figure 3-12: Coil placements relative to cell are shown. MOT coils (gray) create a magnetic quadrupole field parallel to the z-axis. Bias coils (yellow) create a uniform field parallel to the Raman beams (green).

most atoms into the $|4, 0\rangle$ dark state. The final step is an application of resonant microwave π pulse, which flips the atoms from $|4, 0\rangle$ into $|3, 0\rangle$. The microwave signal is supplied by an RF signal generator (IFR 2042).

3.5   Cesium Ground State Detection

Laser-induced fluorescence is used to detect the state of atoms at the end of the interferometer. As discussed previously, this state is a superposition of F = 3 and F = 4 hyperfine ground states, and the probability of finding an atom in either state is related to the interferometer phase.

The readout sequence starts with a 500 μs probe beam, which is tuned to the F = 4 → F' = 5 transition. The fluorescence generated by atoms that decay back to F = 4 is measured with a photodetector (Thorlabs PDA36A). The integrated photodetector voltage signal V_{F4} corresponds to atoms found in F = 4. After measuring the F = 4 population, the readout beam is used again to push the F = 4 atoms out of the interaction region. Then, a repump light is applied to move the remaining atoms from F = 3 to F = 4. Then a second 500 μs probe beam is applied, which should

now generate fluorescence corresponding to atoms initially found in F = 3. The photodetector measures this voltage signal as V_{F3}.

This reading is then adjusted by subtracting light and atom background signals. Scattered light background is taken without the MOT coils on before readout, and atom background is taken with MOT coils on. Interferometer pulses are included in neither sequence. The adjusted populations are

$$P_4 = V_{F4} - AtomBG_4 - (LightBG_4)(I_4) \tag{3.2}$$

$$P_3 = V_{F3} - AtomBG_3 - (LightBG_3)(I_3) \tag{3.3}$$

where $AtomBG_n$ is the atom background measured for the integrated nth fluorescence pulse, $LightBG_n$ is the average scattered light per integrated probe power from the nth pulse, and I_n is the integrated probe power from the nth pulse.

Then, the normalized transition probability to F = 4 is $\frac{P_4}{P_4+P_3}$.

An alternative measurement of normalized F = 4 population is without blowing away F = 4 atoms before repumping the F = 3 atoms, so the final fluorescence voltage will reflect the total population of both F = 4 and F = 3. However, this procedure is not as accurate as the former one, because some F = 4 atoms may be scattered out of the interaction region by the first readout pulse.

3.6   Magnetic Shielding

The clock state Zeeman shift has a quadratic dependence on field strength, so stray magnetic fields or field fluctuations may shift the hyperfine splitting frequency, which reduces the stability of atomic timekeeping. Therefore, magnetic shielding is added to reduce the influence of stray magnetic fields.

The efficiency of magnetic shielding is determined by the permeability of the material, thickness of the shield, shape and size of the shield, and the number of shield layers [20]. Shielding factor is a ratio of the magnetic field strength outside of
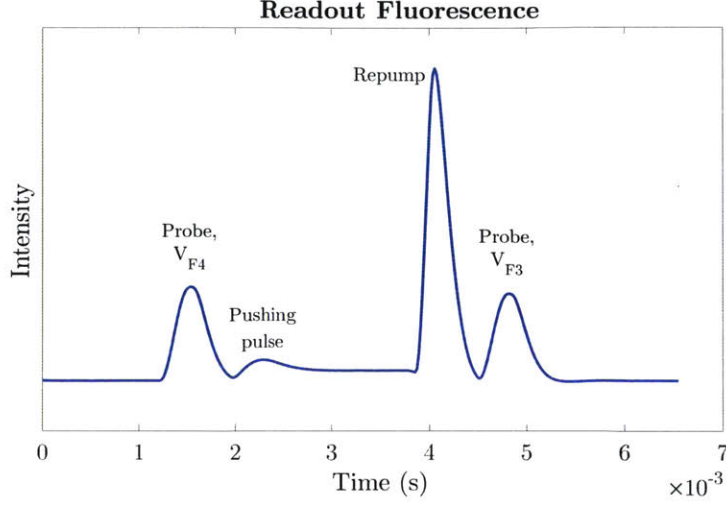
Figure 3-13: Readout fluorescence signal captured by photodetector at the end of the interferometer, lasting about 4 ms. Integrating the first feature gives the population of atoms found in F = 4, V_{F4}. The second feature is the pushing pulse, to remove these atoms from the interaction region. The third is a repump pulse, to transfer F = 3 atoms into F = 4 so they can be read by the final probe pulse as V_{F3}.

shield over that of the inside of shield.

$$S = \frac{B_{out}}{B_{in}} \tag{3.4}$$

Where S is the shielding factor, B_{out} is the magnetic field strength on the outside of the shield, and B_{in} is the magnetic field strength on the inside of shield.

For a single layer, spherical shield, the shielding factor can be written as

$$S = \frac{1}{9\mu} \left[(2\mu + 1)(\mu + 2) - 2 \left(\frac{v}{V} \right) (\mu - 1)^2 \right] \tag{3.5}$$

where v and V are the volumes encompassed by the inner and outer walls of the shield, respectively. It can be assumed that permeability μ of the material is $\gg 1$. For the Mu-metal used in this experiment, this is reasonable because $\mu \sim 10^5$. It can also be assumed that our walls are thin. In that case, this equation reduces to

$$S = 1 + \frac{2}{3} \frac{\mu t}{R} \tag{3.6}$$
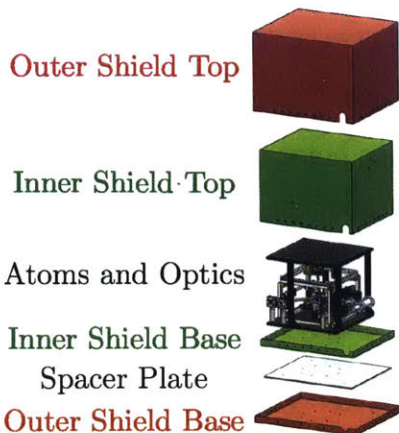
Figure 3-14: Two layers of magnetic shielding enclose the experiment to protect it from stray magnetic fields.

for a sphere, where t is the shield thickness, and R is the shield radius. For a cube, the shielding factor can be written [21]

$$S = 1 + \frac{4}{5}\frac{\mu t}{a} \tag{3.7}$$

where a is the length of the cube side.

The above equations show that shield factor is linearly proportional to the thickness of shield; however, it can be seen from equation 3.5 that a single-layer shield has a maximum potential shield factor of $S = (2/9)\mu$ for an infinitely thick shield. A multi-layer thin-walled shield is much more effective than a single-layer thick-walled shield. The multi-layered shielding factor S_{tot} is proportional to the products of individual shielding factors S_i

$$S_{tot} = S_n \prod_{i=1}^{n-1} S_i \left[1 - \left(\frac{D_{i+1}}{D_i} \right)^k \right] \tag{3.8}$$

where n is the total number of layers, k is a geometry factor (e.g., k = 3 for sphere), and D_i is the average diameter of the ith layer of shielding.

Mu-metal has high permeability and is used to fabricate double-nested rectangular prisms covering the MOT system (Figure 3-14). Each shield layer consists of a shallow base and a top that can snugly fit in the base.

A spacer plate is placed between the two bases to ensure optimal separation between the two shield layers, and to physically mount the shield bases. In addition, the shield bases have clearance holes that enable the system to be mounted directly to a breadboard rather than to the shield bases. Otherwise, the stress on the shields from the weight of system would distort them and reduce their efficacy.

3.7 Apparatus Size Reduction

One of the goals for atomic timekeeping is compactness, and size reduction of the system is still underway. The first system has a volume of $18'' \times 18'' \times 15'' = 4860$ in^3.[1] The second system is cylindrical, with a diameter of 8.35" and a height of 7.45". So, the new model takes only 8.4% the volume of the previous one. Although most of the experiments in this thesis were carried out on the first system, the writer was heavily involved in the design and build of this new model, named the Compact Laser Atom Sensor Prototype (CLASP).

The quartz vacuum cell, collimators, and optical fibers have remained the same between the systems for risk mitigation, and impose the minimum size constraint of the second system. One main change has been elimination of the large rectangular nulling coils outside of the MOT and bias coils in favor of cylindrical cosine windings to cancel ambient fields. The cylindrical cosine windings also allow the two layers of shielding to become cylindrical. Another main change is the advent of a copper pinch-off tube in the second system to replace the seldom-used valve to the turbo pump in the first system. Other changes are more minor, such as reduction of fluorescence photodetector size, and custom-made mounts for optical components.

---

[1]This volume does not reflect shield dimensions, which encompass a greater volume. Note also that the size of the system does not include the laser frequency generation optics, described in section 3.3.

Chapter 4

Experimental Results

4.1 Atomic Timekeeping

Atomic timekeeping with stimulated Raman transitions or Raman adiabatic rapid passage must take into account the multiple sources of systematic perturbations and random errors. As discussed in chapters 2 and 3, the interaction between the Raman laser and atoms causes an AC Stark shift, which perturbs the energies of the hyperfine levels. The presence of magnetic fields also affects the hyperfine levels due to the Zeeman shift. In addition, the Doppler shift experienced by fast-moving atoms also impacts their interrogation. The Doppler effect has been minimized by laser cooling of cesium atoms to about 20 μK in this thesis.

4.1.1 Characterization and Cancellation of AC Stark Effect

The AC Stark effect was characterized in two different methods. One method used a detuning scan, in which a single Raman pulse of duration $t_\pi = \pi/\Omega$ was applied, with varying detuning δ. This detuning was swept from several hundred kHz off resonance symmetrically through resonance over the course of several shots, and the frequency for the peak transition probability was located. Usually, the frequency of maximum transition probability is shifted from the nominal atomic resonance frequency due to the AC Stark shift. The intensity ratio between the two Raman frequencies was then
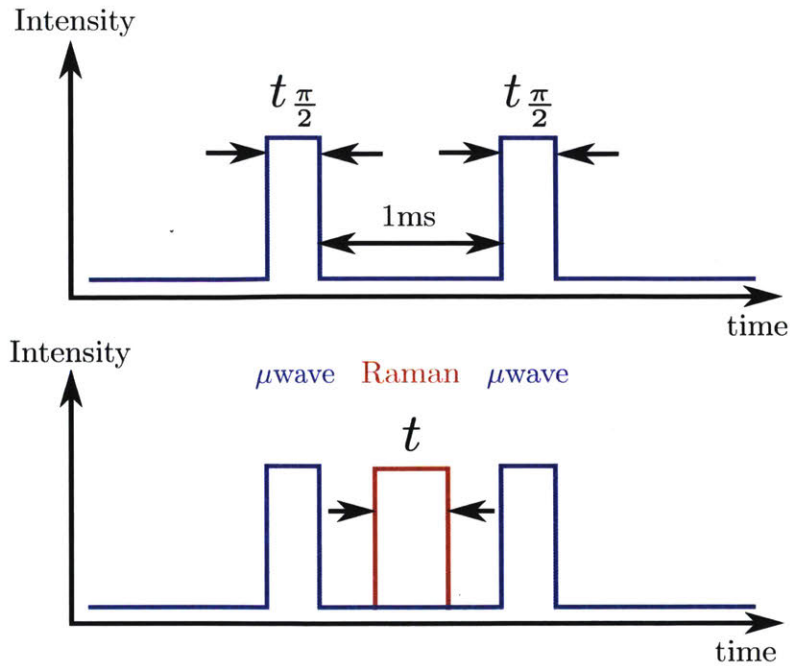
Figure 4-1: Ramsey sequences used to characterize the differential AC Stark shift are composed of two microwave $\pi/2$ pulses separated by a dwell time of 0.001 s. The second sequence also includes an off-resonance Raman pulse of time t between the microwave pulses.

adjusted until this frequency coincided with the atomic resonance frequency to within a few hundred Hz.

The second method used two Ramsey sequences and compared the Ramsey phase differences between them. One Ramsey sequence is composed of two $\pi/2$ microwave pulses generated from the Symmetricom 5071A separated by a dwell time T. The other Ramsey sequence is identical, but also includes a far off-resonance Raman pulse sandwiched between the two microwave pulses (Figure 4-1). This Raman pulse would be unable to stimulate Raman transitions, so any Ramsey phase shift seen would be almost entirely due to the differential AC Stark effect.

As addressed in chapter 2, the interferometer is run at the $\Phi_0 = \pi/2$ point due to its maximal sensitivity at this phase. The dwell time is set to $T_0 = 0.001$ s. This short dwell time minimizes the effects of residual light shifts in the dark or frequency instability in the microwave circuit that may contribute to Ramsey phase shift. As mentioned,

$$\Phi = \delta T \tag{4.1}$$

In this case, the Raman detuning $\delta_0 = 250$ Hz. The experimental result for this detuning is 249 Hz, which is consistent with this calculation. For the microwave Ramsey sequence with Raman pulse sandwiched between the two microwave pulses, the Ramsey phase is $\Phi_{withRaman} = \Phi_0 + \Phi_{AC}$. In the sequence without Raman, $\Phi_{noRaman} = \Phi_0$. The difference in the Ramsey phase between the two sequences $\Delta\Phi_{total} = \Phi_{withRaman} - \Phi_{noRaman}$ is (using equation 2.33)

$$\Delta\Phi_{total} = \Phi_{AC} \tag{4.2}$$

$$= 2\pi\delta_{AC}t = \frac{2}{C}dP \tag{4.3}$$

where δ_{AC} is the differential AC Stark shift in Hz, t is the Raman pulse length, and C is the interferogram contrast. Various Raman pulse lengths were used in order to calculate the AC Stark shift with a linear fit before experiments. An example of this is shown in Figure 4-2.

The first method was used to cancel the AC Stark shift, and then the second method was used to check for residual AC Stark shift. In practice, the first method was used alone most of the time.

4.1.2 Ramsey Sequences

For stimulated Raman pulses, the Ramsey sequence is two $\pi/2$ pulses with a dwell time T of more than 10 ms.

After the cancellation of differential AC Stark shift using an approximate π pulse, the Rabi rate and the duration of the $\pi/2$ pulse were determined from Rabi flopping. A resonant Raman pulse was applied to the atoms, and the pulse length was incremented uniformly over several shots. A sinusoidal transition probability versus the duration of Raman pulse was mapped out (Figure 4-3), and Rabi rate and the length
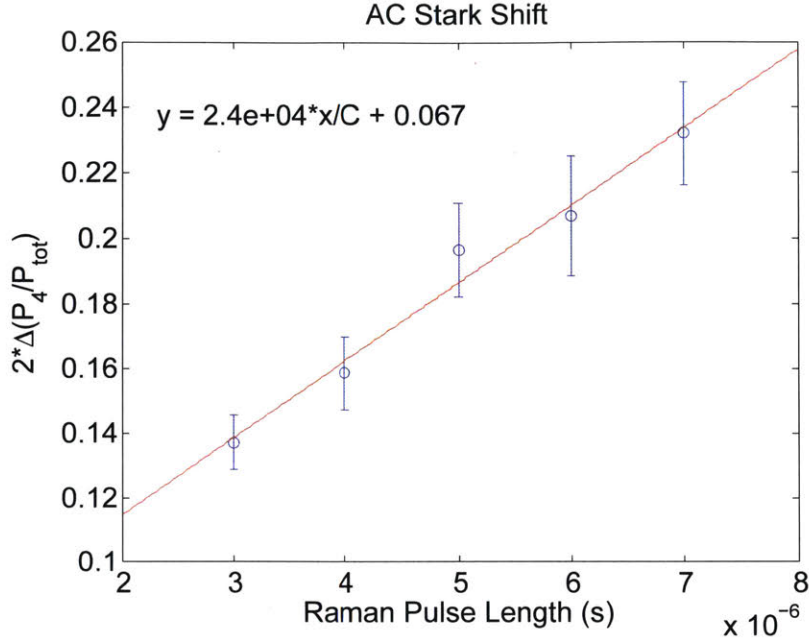
Figure 4-2: Plot of Ramsey phase difference verses Raman pulse length. The slope of the linear fit gives the AC Stark shift.

of $\pi/2$ pulse were computed from these data. Compared with the dwell time, the Raman π pulse is much shorter and usually on the order of 5-10 μs. Damping occurs due to decoherence processes over the long pulse duration.

Then, standard Raman and ARP Raman pulses of length $t_{\pi/2} = \frac{\pi/2}{\Omega}$ and $26t_{\pi/2}$ respectively were used in $\pi/2 - \pi/2$ Ramsey sequences to produce Ramsey fringes (Figure 4-4). These data were analyzed to identify the mid-fringe phase value using equation 2.33.

4.1.3 Magnetic Shielding

Kotru [8] pointed out that fluctuations of ambient stray magnetic fields caused Ramsey phase jitter, and therefore negatively affected the stability of atomic timekeeping for both stimulated Raman and Raman adiabatic rapid passage (ARP) interferometers. The magnetic field instability was the dominant noise source for measurement times greater than about ten seconds, and was characterized by spectroscopy of the resonance frequency between the $m_F = 1$ magnetic sublevels of the F = 3,4 hyperfine

Figure 4-3: Pulse length scan of Raman pulse from 0 to $31\mu s$. Rabi rate is calculated in this instance using fit data to be 100kHz.

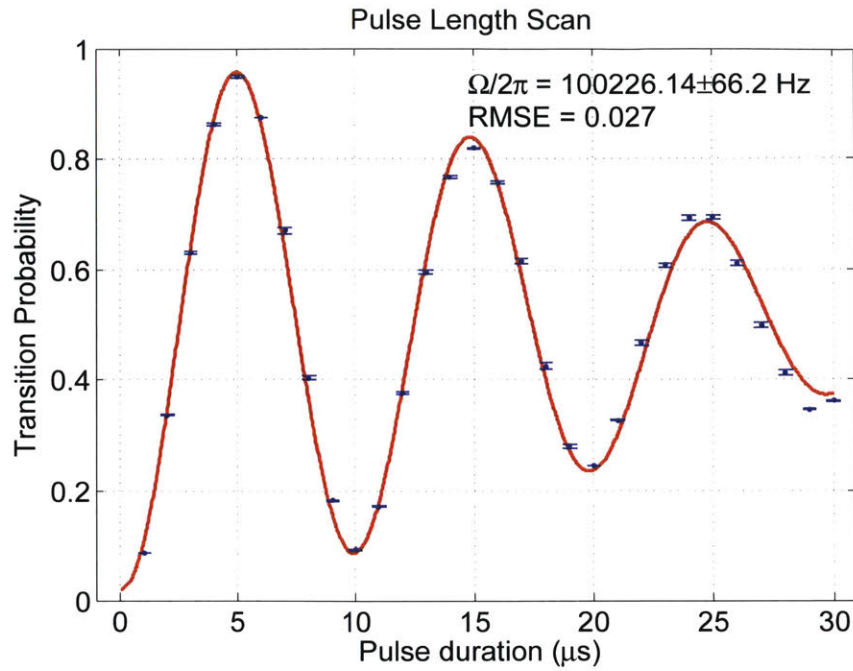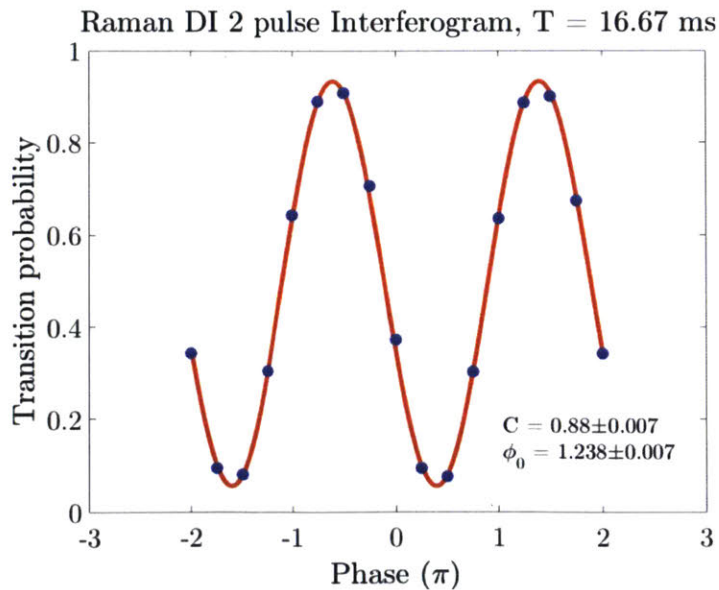Figure 4-4: Interferogram taken using two standard Raman pulses in a Ramsey sequence with dwell time 16.67 ms, plotted as a function of phase difference between the two pulses. Contrast is 88%.

states, which have a first-order sensitivity to the Zeeman shift of 700 kHz/Gauss. In this thesis, passive magnetic shielding was used to suppress the effect of environmental magnetic fields.

Allan deviation [22] is widely used to assess the stability of atomic clocks. Unlike standard deviation, which measures the dispersion from the mean value of all measurements, Allan deviation focuses on the difference between the consecutive measurements. A low Allan deviation is an indicator of good stability.

Allan deviation $\sigma_y(\tau)$ is the square root of the Allan variance, which is defined as

$$\sigma_y^2(\tau) = \frac{1}{2(N-1)} \sum_{i=1}^{N-1} (y_{i+1} - y_i)^2 \tag{4.4}$$

In the clock experiment, $y_i = (\omega_i - \omega_{HFS})/\omega_{HFS}$ is the ith measured fractional frequency difference with ω_i as the ith measured frequency. N is the total number of measurements, and τ is the time interval between consecutive measurements.

One advantage of Allan deviation over standard deviation is that various types of noise processes can be identified by averaging adjacent values of y_i for longer time intervals τ (e.g., $10^0 - 10^4$ seconds). Allan deviation for the above grouped measurements is expressed as

$$\sigma_y(\tau) = \sqrt{\frac{1}{2(N-1)} \sum_{i=1}^{N-1} (\bar{y}_{i+1} - \bar{y}_i)^2} \tag{4.5}$$

where $\bar{y}_i$ is the average value of the ith group of measurements over time interval τ.

Allan deviation is usually presented as a log-log plot of $\sigma_y(\tau)$ versus τ. In many cases, several types of noise processes can be identified on the plot based on the slopes of the different plot regions, depicted in Figure 4-5. White noise is a type of stationary noise which fluctuates around a baseline that does not change over time. So, averaging data suffering from white noise over a longer period of time will yield better precision, as can be seen from the -0.5 slope which characterizes it. After a certain τ, the white noise will be fully averaged out and optimal stability is
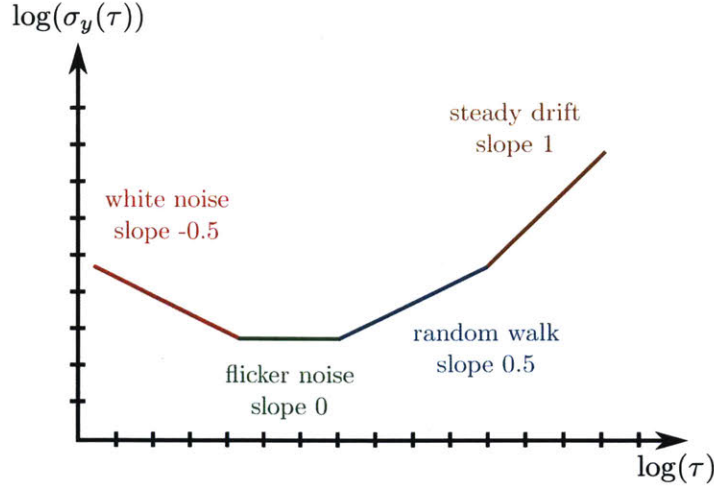
Figure 4-5: An Allan deviation plot can characteristic different noise types using the slope of the plot.

achieved at the flicker floor. This is also called the "bucket" or fractional frequency uncertainty. Over longer periods of time, random walk and drift processes begin to dominate. These are systematic noises, which alter the baseline about which white noise fluctuates. So, averaging data over these time scales will yield worse precision, as seen from the 0.5 and 1 slopes characterizing random walk and drift respectively.

Another advantage of using Allan deviation over standard deviation is that when random walk and drift noises dominate, standard deviation diverges as $N \to \infty$. Allan deviation circumvents this divergence problem.

Raman ARP data were acquired with magnetic shielding. From the phase data, fractional frequency difference was obtained via the relation

$$y = \frac{\Phi}{\Phi_{tot}} = \frac{2}{C} \frac{P_4}{P_{tot}} \frac{1}{\omega_{HFS}T} \tag{4.6}$$

The raw frequency data are shown in Figure 4-6 before they are processed into Allan deviation via equation 4.5 in Figure 4-7 (blue line). The stability is $\sigma_y(1s) \sim 7 \times 10^{-12}$ and $\sigma_y(100s) \sim 2 \times 10^{-12}$. In comparison, Raman ARP data without magnetic shielding [8] has a stability of $\sigma_y(1s) \sim 1.5 \times 10^{-11}$ and $\sigma_y(100s) \sim 6 \times 10^{-12}$.

The clock transition Zeeman shift is 427.45 Hz/G^2. With a bias field of 183 mG in the shielded data, the second order Zeeman splitting induced in the $m_F = 0$ ground

71
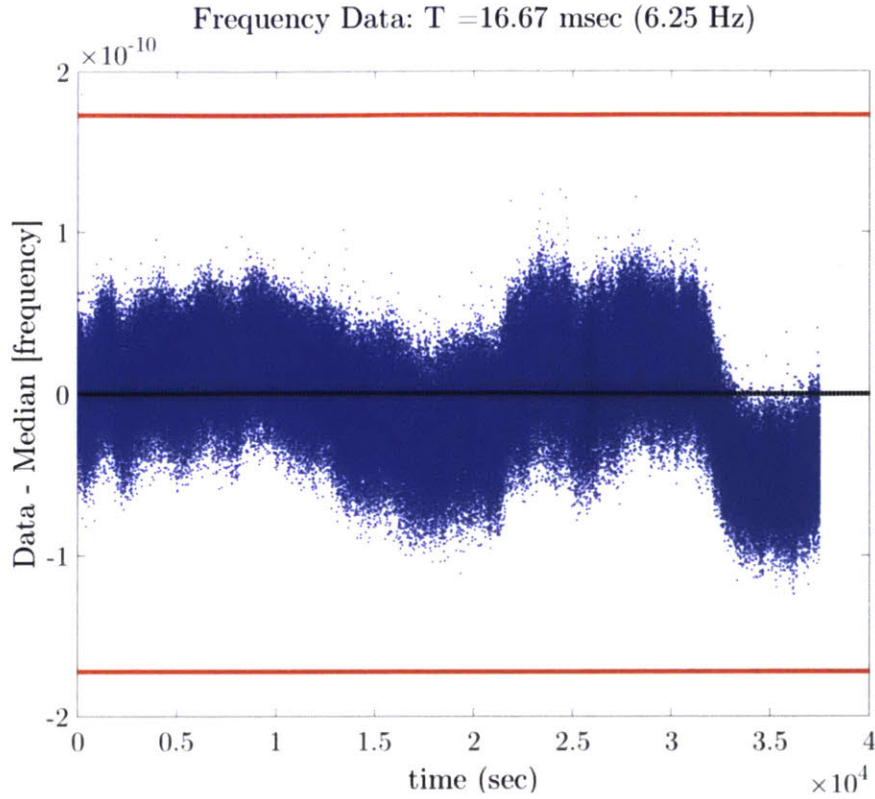
Figure 4-6: Fractional frequency difference plotted as a function of time over one experiment, as deviation from median frequency.
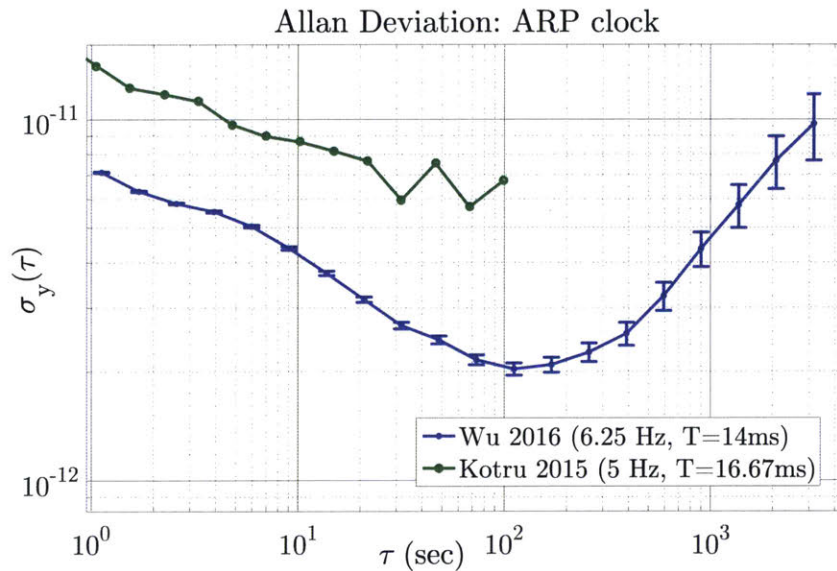
Figure 4-7: Allan deviations of fractional frequency measurement using Raman ARP pulses with magnetic shielding (blue) in comparison with the ARP data trend without magnetic shielding (green). Note both experiments have similar relatively high data rates, 6.25 Hz and 5.0 Hz respectively. Higher data rates could be employed, and were limited in these experiments by hardware limits on data acquisition rates.

states would be 14 Hz. Kotru found that after $\tau = 10s$, clock stability is related to magnetic field fluctuations [8]. To cause the Allan deviation at 20 seconds of 8×10^{-12}, we can deduce from equation 4.5 that fluctuations of about 3 mG are required in the non-shielded 87 mG field, if magnetic fluctuations were the sole source of noise.[1]

The Allan deviation bucket in the magnetically shielded data is at about $\sigma(200s) = 2 \times 10^{-12}$. This corresponds to a 0.24 mG field fluctuation, which is about 0.13%. This level of fluctuation could have been caused by, e.g., fluctuations in the power which supplied the bias field within the shields. In magnetic coils, the magnetic field produced is proportional to input current, and the power supply used has a current programming accuracy of 0.15% + 20 mA [23].

Other factors could have contributed to this discrepancy. There could have been a fluctuation of the interrogation time $T_d = T + \Delta T$ from shot to shot, which would have had impact on the phase $\Phi = \delta(T + \Delta T)$. With operation close to resonance, the $\delta \Delta T$ term would give a very small contribution. To account for an apparent frequency fluctuation of 2×10^{-12}, the fractional variance in T would have to be of order 2%, or nearly 0.3 ms. Timing fluctuations are of order 0.1 μs, so timing fluctuations cannot account for the Allan deviation bucket.

An important limit to the 6.25 Hz data is the Symmetricom 5071A reference clock, which has a reported stability of $\leq 5 \times 10^{-12}$ at $\tau = 1s$ [24]. The 7×10^{-12} at one second of the magnetically shielded data is the combination of the ARP clock noise and the Symmetricom reference added in quadrature. This would be observed if, e.g., both the Symmetricom and the ARP clock data had Allan deviation of about 5×10^{-12} at one second. Thus, it can be seen that Allan deviation at small τ is significantly affected by reference noise, and the ARP clock actually has a short term stability better than 7×10^{-12} at one second. This is a significant result.

One way to improve measured stability is via closed-loop operation of the clock. It is noted that so-called open loop operation can contribute to long term frequency drift. By "open loop", it is meant that the atoms are used passively to measure the frequency difference between the atomic resonance and the reference oscillator. Changes in the

---

[1]For reference, the Earth has a field of 250 to 650 mG.

mean value or contrast of the interferogram (Figure 4-4) can be mistaken for frequency variation in open loop operation. Closed loop operation, wherein a local oscillator is tuned to remain in resonance with the atoms, can be designed to be essentially invariant under the slow changes in interferogram mean value or contrast. In closed loop operation, a tunable oscillator outputs a frequency signal which is used to drive the Raman lasers, which interrogate the atoms. Then, the atoms would report the difference between the laser frequency they see and their own ω_{HFS}, which then is used to tune the oscillator. The quartz crystal oscillator should have low noise, ideally in the low 10^{-12} range at one second. An oven-controlled quartz crystal oscillator with, e.g., $\sigma(1s) = 5 \times 10^{-12}$ may be purchased commercially [25].

4.1.4   ARP Raman Pulse vs Standard Raman Pulse

In order to effectively compare Raman ARP and standard Raman clocks, two Ramsey sequences were interleaved in the experiment. This means that a measurement would be made using an ARP sequence, then another using a Raman sequence, then ARP, etc. This simultaneous scheme eliminates some undesirable effects arising from the independent experiments of Raman ARP and standard Raman transitions, since t_π, environmental magnetic field, AC Stark shift, and other factors fluctuate from day to day.

Use of ARP in atom interferometry was recently developed at Draper Laboratory. Compared with standard Raman pulses, using ARP Raman pulses was shown to reduce the Ramsey phase sensitivity to the AC Stark shift by about two orders of magnitude [7]. Further investigation of the stability of atomic timekeeping with ARP Raman pulses as opposed to standard Raman pulses was carried out in this thesis. Several interleaved ARP and standard Raman measurements show that stability is superior when using ARP, shown in figure 4-8. These data were taken at 2×0.89 Hz, though effective data rate 0.89 Hz is used to plot data for all ARP measurements, or all standard Raman measurements. Dwell time was set to T = 16.67 s and bias field was 183 mG.[2] Although stability improvement is not uniform throughout all values

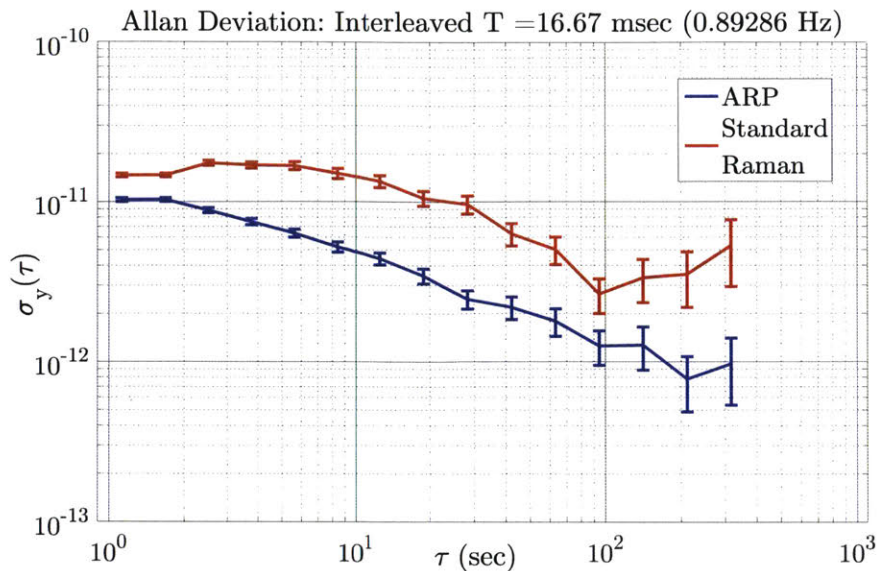---

[2]measured with Nicole Pomeroy.

Figure 4-8: Interleaved ARP and standard Raman measurement data are plotted in blue and red, respectively, taken with magnetic shielding. Effective data rate $\frac{1}{1.12s} = 0.89$ Hz is that between each ARP measurement or standard Raman measurement. Data rate between consecutive measurements is $\frac{1}{0.56s}$. The relationship between data rate and short terms stability will be further described in Section 4.1.5.

of τ, it is roughly a factor of 3 better when comparing Allan deviation values at $\tau = 10$ s.

The stability improvement seen when using ARP may indicate that AC Stark shift is a limiting factor when using standard Raman. The AC Stark shift fluctuations may come from power instabilities ($\sim 1\%$ power) in the RF signal modulating the EOM.

Placing the results into a larger context, the Allan deviation of ARP Raman is about $\sigma_y(1s) = 7 \times 10^{-12}$ and $\sigma_y(100s) = 2 \times 10^{-12}$, which is much better than the stability of CSAC clocks ($\sigma_y(1s) = 3 \times 10^{-10}$ and $\sigma_y(100s) = 3 \times 10^{-11}$) [4] and better than that of the NIST cold atom double-Λ coherent population trapping clock ($\sigma_y(1s) = 4 \times 10^{-11}$ and $\sigma_y(100s) = 4 \times 10^{-12}$), at a data rate of 19Hz [9].

4.1.5 High Data Rate

Short term stability is enhanced by increasing data rate. In order to explore this possibility, Raman ARP data were acquired at high data rate of 6.25 Hz, and then a new set of data were generated by taking every other point of the above data. The
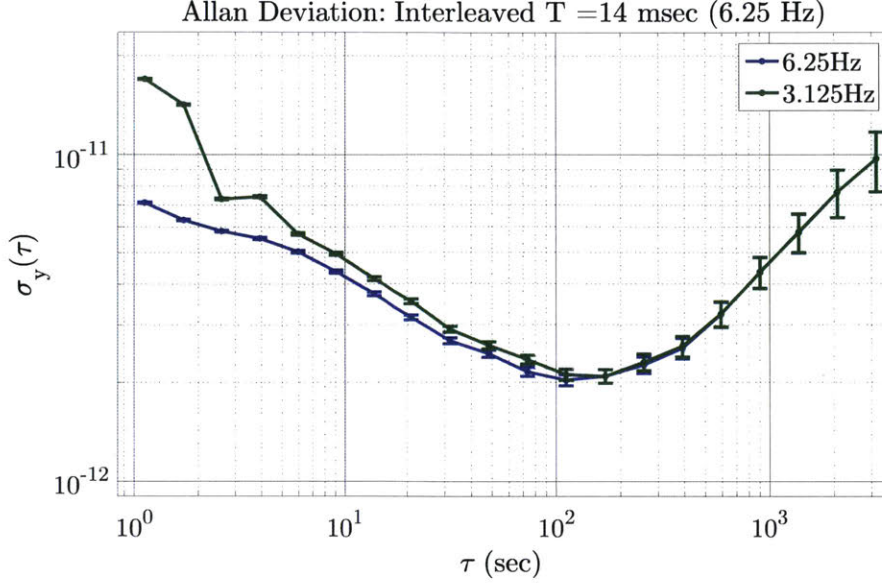
Figure 4-9: Allan deviation plots of ARP Raman data using data rates of 6.25 Hz and 3.125 Hz. The 3.125 Hz data were obtained by taking every other point of the 6.25 Hz data.

new data set has a data rate of 3.125 Hz. The stabilities of two sets of data are shown in Figure 4-9. Clearly, the stability improves with the high data rate when τ is less than 100 s, but there is no difference in stability when τ is more than 100 s.

The improvement of stability is largely due to the dominance of white noise when τ is less than 100 s. Allan deviation has negative slope at relative short τ for most of the stability measurements in this thesis, indicating that white noise is dominant at early times.

In particular for white Gaussian noise, when $\tau = n\tau_0$, the Allan deviation will reduce by

$$\sigma_y(\tau) = \frac{1}{\sqrt{n}}\sigma_y(\tau_0) \tag{4.7}$$

For this reason, white-noise limited stability at low τ may improve by $1/\sqrt{2}$ if the data rate is doubled from 3.125 Hz to 6.25 Hz. This is comparable to the undersampled experimental result in Figure 4-9. As expected, increasing data rate has no effect on stability at high τ .

This effect can be seen when comparing the 0.893 Hz ARP Raman data from Fig-
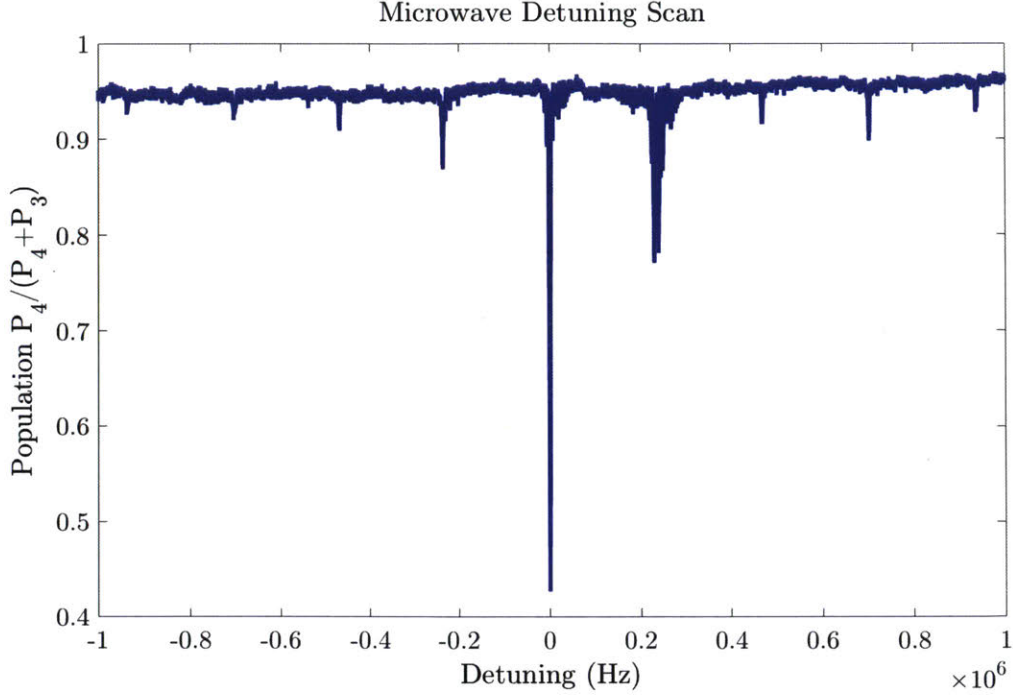
76

Figure 4-10: Microwave detuning scan in miniature apparatus from $\omega_{HFS} - 1$ MHz to $\omega_{HFS} + 1$ MHz. The majority of atoms are within the magnetically insensitive clock state, closest to zero detuning.

ure 4-8 and the original 6.25 Hz data from 4-9. From the experimental data, the 0.893 Hz data has stability of 1.03×10^{-11} and the 6.25 Hz data has stability 6.3×10^{-12} at 1.7 s, which gives $\sigma_y(7\tau_0) = \sigma_y(\tau_0)/1.6$. The factor given by purely white-noise limited stability would be $1/\sqrt{7} = 1/2.6$. This indicates that other processes are responsible for frequency instability at this low τ, further seen by the slope of more than -0.5 at $\tau < 10s$, though white-noise processes were definitely a contributing factor. At 6.3×10^{-12}, a significant contribution also arises from the reference clock used to generate Raman pulses, which has a reported $\sigma(1s) \leq 5 \times 10^{-12}$ [24]. Estimating the measured one second Allan variance of the Raman clock to be the sum of the Raman and Symmetricom Allan variance (assumed to be 5×10^{-12} at one second) in quadrature, the actual Allan deviation at one second would be 3.8×10^{-12}.

4.2 Accelerometry

Accelerometry is planned for the new miniature CLASP apparatus, which is currently in the testing and adjustment stage. So far, the vacuum system and MOT are fully operational. Cesium atoms have been successfully cooled and trapped at the center of the MOT.

State preparation of the atoms in this system, as in the larger test bed, manipulates atoms into the $|F = 4, m_F = 0\rangle$ state using lasers and then to the $|F = 3, m_F = 0\rangle$ state using microwaves. In order to test the efficiency of this preparation, the microwave frequency was incremented through a wide range around resonance, shown in Figure 4-10. The largest feature is that near zero detuning, which corresponds to the transition from $|4, 0\rangle$ to $|3, 0\rangle$ driven by the microwaves. This shows that the majority of atoms reside within the magnetically insensitive state, as desired. The other features, spaced 230 kHz apart, correspond to transitions from magnetically sensitive states, which have Zeeman-shifted resonance frequencies. Zeeman splitting between adjacent magnetic sublevels of the F = 4 state is 0.35 MHz/G, which gives a field of 660 mG based on the data [10].

After successful state preparation, the next step is interferometry. Doppler-sensitive Raman optics have been implemented. A new Raman laser board has been built to replace that in Figure 3-9 to facilitate Doppler-sensitive operation. A preliminary interferogram was obtained, shown in Figure 4-11 [26]. The data display a low contrast of about 11%, which indicates lack of efficiency in Raman beams driving the atoms. These Raman lasers are currently undergoing optimization.

The miniature system will operate in both Doppler-sensitive, Doppler-insensitive, and combined modes. This allows it to support both precision one-dimensional accelerometry and timekeeping. For accelerometry, a second system would be built, identical to the first, to enable "back-to-back" measurements–one system can perform interferometry to measure accelerations while the other is trapping atoms in preparation to do so. Magnetic shields and mechanical parts were obtained for the second system. It is desired to test CLASP in various orientations with respect to
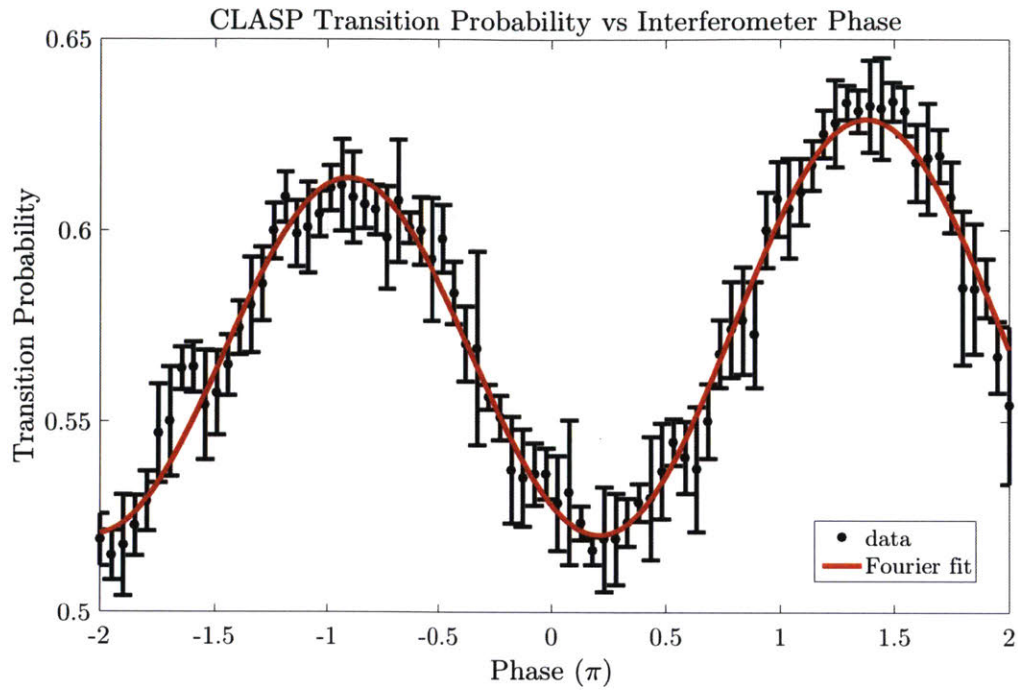
Figure 4-11: Interferogram obtained from CLASP system. Data are in black, and Fourier fit is in red. Contrast is about 11%.

gravity, mounted on an indexing head, to ultimately produce a technology readiness level (TRL) 4 or more apparatus. [27]

Chapter 5

Conclusions and Future Work

Atomic fountain clocks for international time standards are room-sized and operated in lab controlled environments. Compact atomic clocks such as the CSAC are not accurate enough for primary reference and only serve as secondary timing references. There remains an unfulfilled need for compact atomic clocks of primary reference. This thesis explored atomic timekeeping by interrogating cold cesium atoms in a highly vacuumed miniature cell with laser pulses.

A new laser pulse scheme, Raman ARP, was recently developed at Draper Laboratory; it has been shown that Raman ARP can significantly suppress the Ramsey phase sensitivity to AC Stark shift. This thesis further investigated the stability of atomic timekeeping using Raman ARP in comparison with the standard Raman transition. When using ARP Raman pulses, the stability was enhanced by a factor of $\sim$3 compared to standard Raman pulses.

Since the original study of Raman ARP at Draper Laboratory was not magnetically shielded, this thesis explored the timekeeping stability improvement with magnetic shielding. A double layered shielding of Mu-metal improved the ARP stability by a factor of 2 to 3.

Increasing the data rate also enhanced short term stability. The experimental results show that adopting a data rate of 6.25 Hz improved the stability by a factor of about 1.6 in comparison with a data rate of 0.893 Hz.

Further data rate increase may be feasible, by taking advantage of atom recapture,

which could be as high as 85% to 95% which has been demonstrated at data rates of 50 to 330 Hz [28]. In the current system, an increase to, e.g., 31 Hz would give 16 ms for interrogation and 16 ms for MOT cooling. Within 16 ms, the MOT will fall fractions of a millimeter, and thermally expand even less. With 10 mm MOT beams, recapture could be feasible.

In general, the Allan deviation when using Raman ARP, magnetic shielding, and high data rate reaches about 7×10^{-12} at 1 second and 2×10^{-12} at 100 seconds, which are more than one order of magnitude better than that of CSACs (3×10^{-10} at 1 second and 3×10^{-11} at 100 seconds). This result is slightly better than that of the cold-atom double-Λ coherent population trapping clock (4×10^{-11} at 1 second and 4×10^{-12} at 100 seconds).

Future work should include a feedback system. The error signals from the Ramsey phase measurements should be fed back to a local oscillator to match the resonance frequency of the cesium atoms, preferably with a more complicated scheme such as A-B mod. In addition, fixing optical intensity of Raman and probe lasers with a control loop may better cancel the effects of AC Stark on clock stability. Further, operation of the clock in closed-loop configuration would remove dependence on the Symmetricom clock and increase stability. Although the author made an attempt at these, they require significant improvement to be effective.

Though operation in dynamic environments necessitates high short-term stability, long term stability may be improved in future work as well. Implementation of this may require periodic recalibration of light background levels and temperature controls.

Bibliography

[1] Richard Stoner, David Butts, Joseph Kinast, and Brian Timmons. Analytical framework for dynamic light pulse atom interferometry at short interrogation times. *J. Opt. Soc. Am. B*, 28(10):2418–2429, Oct 2011.

[2] Michael A. Lombardi. Fundamentals of time and frequency. *The Mechatronics Handbook*, 2002.

[3] Thomas P Heavner, Elizabeth A Donley, Filippo Levi, Giovanni Costanzo, Thomas E Parker, Jon H Shirley, Neil Ashby, Stephan Barlow, and S R Jefferts. First accuracy evaluation of nist-f2. *Metrologia*, 51(3):174, 2014.

[4] Quantum^{TM} SA.45s CSAC. `http://www.microsemi.com/document-portal/doc_download/133305-quantum-sa-45s-csac`. Accessed: 2016-12-8.

[5] N. Belcher, E. E. Mikhailov, and I. Novikova. Atomic clocks and coherent population trapping: Experiments for undergraduate laboratories. *American Journal of Physics*, 77:988–998, November 2009.

[6] Mark Kasevich and Steven Chu. Atomic interferometry using stimulated raman transitions. *Phys. Rev. Lett.*, 67:181–184, Jul 1991.

[7] Krish Kotru, Justin M. Brown, David L. Butts, Joseph M. Kinast, and Richard E. Stoner. Robust ramsey sequences with raman adiabatic rapid passage. *Phys. Rev. A*, 90:053611, Nov 2014.

[8] Krish Kotru. *Timekeeping and accelerometry with robust light pulse atom interferometers*. PhD dissertation, Massachusetts Institute of Technology. Dept. of Aeronautics and Astronautics, June 2015.

[9] F.-X. Esnault, E. Blanshan, E. N. Ivanov, R. E. Scholten, J. Kitching, and E. A. Donley. Cold-atom double-Λ coherent population trapping clock. *Phys. Rev. A*, 88:042120, Oct 2013.

[10] Daniel A. Steck. Cesium D Line Data. Available online at `http://steck.us/alkalidata` (revision 2.1.4, 23 December 2010).

[11] David S. Weiss, Brenton C. Young, and Steven Chu. Precision measurement of the photon recoil of an atom using atomic interferometry. *Phys. Rev. Lett.*, 70:2706–2709, May 1993.

[12] Daniel A. Steck. Quantum and Atom Optics. Available online at `http://steck.us/teaching` (revision 0.11.0, 18 August 2016).

[13] William J. Williams, Mark L. Brown, and Alfred O. Hero. *Uncertainty, information, and time-frequency distributions*, volume 1566, pages 144–156. Publ by Int Soc for Optical Engineering, 1991.

[14] Norman F Ramsey. Experiments with separated oscillatory fields and hydrogen masers. *Reviews of modern physics*, 62(3):541, 1990.

[15] M. Kasevich and S. Chu. Measurement of the gravitational acceleration of an atom with a light-pulse atom interferometer. *Applied Physics B*, 54(5):321–332, 1992.

[16] Giacomo Lamporesi. *Determination of the gravitational constant by atom interferometry*. PhD dissertation, Universit Degli Studi Di Firenze, December 2006.

[17] E. L. Raab, M. Prentiss, Alex Cable, Steven Chu, and D. E. Pritchard. Trapping of neutral sodium atoms with radiation pressure. *Phys. Rev. Lett.*, 59:2631–2634, Dec 1987.

[18] Steven Chu, L. Hollberg, J. E. Bjorkholm, Alex Cable, and A. Ashkin. Three-dimensional viscous confinement and cooling of atoms by resonance radiation pressure. *Phys. Rev. Lett.*, 55:48–51, Jul 1985.

[19] Daryl W. Preston. Doppler-free saturated absorption: Laser spectroscopy. *American Journal of Physics*, 64(11):1432–1436, 1996.

[20] E. A. Donley, E. Hodby, L. Hollberg, and J. Kitching. Demonstration of high-performance compact magnetic shields for chip-scale atomic devices. *Review of Scientific Instruments*, 78(8), 2007.

[21] Slawomir Tumanski. *Handbook of Magnetic Measurements*, chapter 2.14.2, page 106. CRC Press, 2011.

[22] David W Allan. Should the classical variance be used as a basic measure in standards metrology? *IEEE Transactions on instrumentation and measurement*, 1001(2):646–654, 1987.

[23] Agilent Technologies Modular Power System Series N6700 User's Guide. `http://ridl.cfd.rit.edu/products/manuals/Agilent/power%20supplies/CD1/Model/N6700usr.pdf`. 119, Jan 2005. Accessed: 2017-04-12.

[24] 5071a Primary Frequency Standard. `http://www.microsemi.com/document-portal/doc_download/133269-5071a`. Accessed: 2017-04-07.

[25] Vectron OX-045 Oven Controlled Crystal Oscillator. `https://www.vectron.com/products/ocxo/ox-045.pdf`. Accessed: 2017-04-12.

[26] Brian Timmons. Clasp interferogram. Private communication.

[27] Richard Stoner, Nicole Pomeroy, and Justin Brown. Compact Laser Atom Sensor Prototype (CLASP) Design Summary. Memorandum, November 2014.

[28] Grant W. Biedermann Hayden J. McGuinness, Akash V. Rakholia. High data-rate atom interferometer for measuring acceleration. *Applied Physics Letters*, 2012.